Cell Stem Cell

Article

High-content screening of organoids reveals the mechanisms of human pancreas acinar specification

Graphical abstract

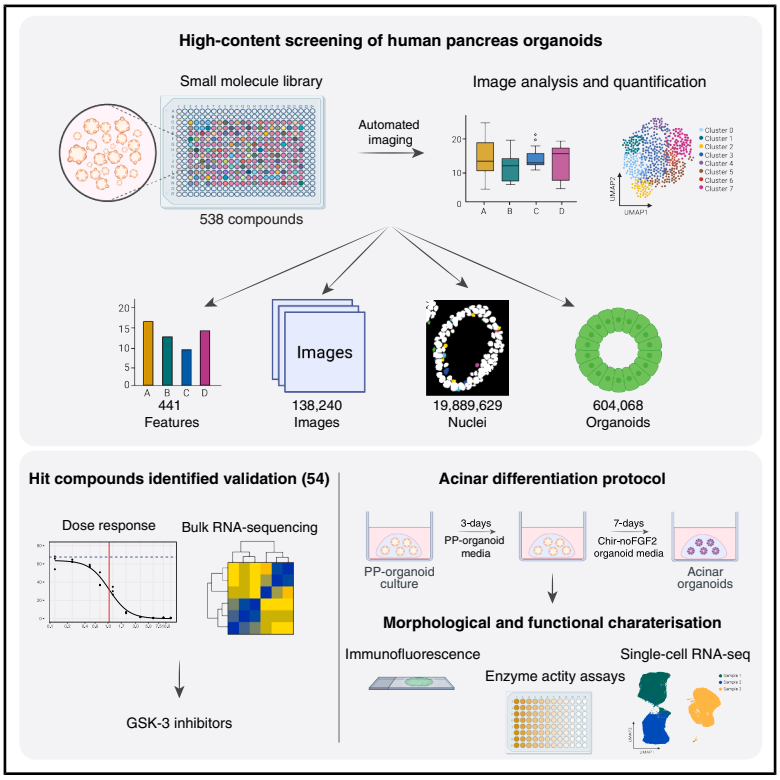

Authors

Rashmiparvathi Keshara, Karolina Kuodyte, Antje Janosch, ..., Rico Barsacchi, Yung Hae Kim, Anne Grapin-Botton

Correspondence

botton@mpi-cbg.de

In brief

Keshara et al. conducted a high-content screen on pancreas organoids that identified 54 compounds affecting differentiation or morphogenesis. After validating 11 compounds, they focus on Gsk3A/B inhibitors, which, combined with FGF withdrawal, drive acinar cell differentiation, enabling future studies on these cells and their role in cancer initiation in humans.

Highlights

- High-content screen reveals 54 compounds altering organoid shape or differentiation
- Analysis methods robust to organoid heterogeneity are established
- Screen-derived GSK3A/B inhibitors control pancreatic acinar cell differentiation

Keshara et al., 2026, Cell Stem Cell *33*, 325–339
February 5, 2026
https://doi.org/10.1016/j.stem.2025.12.023

CellPress

Cell Stem Cell

CellPress
OPEN ACCESS

Article

High-content screening of organoids reveals the mechanisms of human pancreas acinar specification

Rashmiparvathi Keshara,[1] Karolina Kuodyte,[1,5] Antje Janosch,[1,5] Cordula Andree,[1] Marc Bickle,[1] Martin Stöter,[1] Rico Barsacchi,[1] Yung Hae Kim,[1] and Anne Grapin-Botton[1,2,3,4,6,*]

[1]Max Planck Institute of Molecular Cell Biology and Genetics, Dresden 01307, Saxony, Germany
[2]Center for Systems Biology Dresden, Dresden 01307, Germany
[3]Cluster of Excellence Physics of Life, TU Dresden, Dresden 01062, Germany
[4]Paul Langerhans Institute Dresden of the Helmholtz Zentrum München at the University Clinic Carl Gustav Carus of Technische Universität Dresden, Helmholtz Zentrum München, Neuherberg 85764, Germany
[5]These authors contributed equally
[6]Lead contact
*Correspondence: botton@mpi-cbg.de
https://doi.org/10.1016/j.stem.2025.12.023

SUMMARY

Organoids derived from pluripotent stem cells have emerged as powerful models to study human development. To investigate signaling pathways regulating human pancreas differentiation and morphogenesis, we developed a high-content, image-based screen and quantitative multivariate analysis pipelines robust to heterogeneity to extract single-cell and organoid features using pancreatic progenitor organoids. Here, we identified 54 compounds affecting cell identity and/or morphological landscape. Focusing on one family of compounds, we found that glycogen synthase kinase 3α/β (GSK3A/B) inhibition via wingless/int-1 (WNT) signaling has a reversible effect on cell identity, repressing pancreatic progenitor markers and inducing a poised state in progenitors transitioning to acinar cells. We show that additional fibroblast growth factor (FGF) repression enables further differentiation of acinar cells, recapitulating pancreatic acinar morphogenesis and function. The ability to produce acinar cells is valuable for future studies on pancreatic exocrine function and cancer initiation in humans, as acinar cells are thought to be an important cell of origin for pancreatic adenocarcinoma.

INTRODUCTION

Organoids have emerged as a valuable model system to investigate the mechanisms of human development, organ regeneration, function, and disease progression.[1–3] Organoids derived from patient tissues or generated by genetic engineering enable studying how specific proteins or their variants affect these processes.[4] Going beyond single genes, the ease of producing large amounts of material by the expansion of organoids enables multiplexing and studying many genes at a time.[5–7] Combining such investigations on many genes with single-cell sequencing, a global molecular understanding of the effects of perturbations can be inferred. While extremely powerful, this approach does not provide information on morphological or spatial consequences of gene perturbations. For this purpose, high-content image-based screens are more suitable.[8–12] However, they pose challenges in the scale of their implementation and analysis and have so far been underexplored, particularly to study pathways affecting human development. Moreover, developing analysis pipelines robust to the frequent heterogeneity observed in organoids is of utmost importance.

Here, we conducted a high-content screen to investigate the mechanisms of human pancreas development, focusing on both differentiation and morphogenesis. The adult pancreas is composed of acinar and ductal exocrine cells executing digestive functions and 5 types of endocrine cells releasing hormones involved in digestion and glucose homeostasis. These cells form developmentally from pancreatic progenitors (PPs).[13] PPs can be produced from human pluripotent stem cells (hPSCs) and expanded as organoids.[14,15] With readouts for cell identity and morphology, we screened the PP organoids against a library of small molecules targeting kinases and pathways important in stem cells. We developed analysis methods that would identify changes in individual cell identity or more global identity shifts in organoids, as well as readouts of individual cell shape and organoid shape. We identified 54 compounds affecting at least one of the 441 phenotypic features and focused on inhibitors of glycogen synthase kinase 3 (GSK3) among the validated pathways. We found that GSK3 inhibition via WNT signaling has a global reversible effect repressing multiple PP markers and initiating acinar differentiation. We also identified an additional control, fibroblast growth factor (FGF) suppression, that promotes further acinar differentiation,

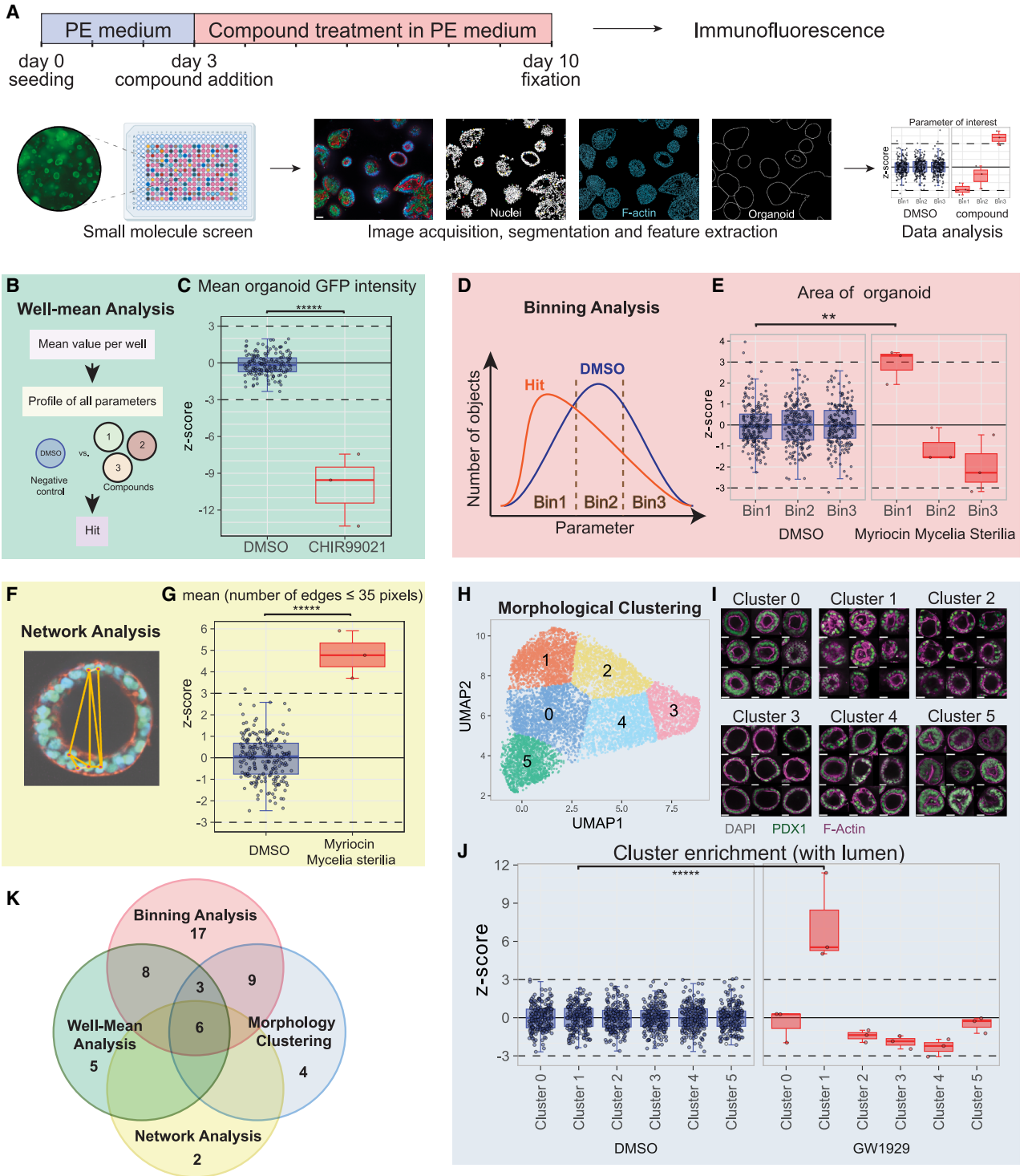

Figure 1. Image-based morphological screening assay for PP organoids

(A) Schematic representation of the experimental protocol for the image-based screening of PP organoids. Seeded PP-cells formed organoids that expanded in pancreatic epithelium (PE) medium, and the compounds were treated from day 3 onward. Fixed organoids on day 10 were stained with DAPI and phalloidin. Images were acquired with an automated spinning disc microscope. Images were segmented, and features of interest were extracted for quantification and hit selection. Created with BioRender.com.

(B–J) Four pipelines for image analysis.

(legend continued on next page)

uncovering the multistep mechanisms of human acinar cell specification from PSCs.

RESULTS

A screening pipeline identifies morphological and differentiation extremes in a progenitor landscape

To easily assess cell identity, we generated a double reporter H9 human embryonic stem cell (hESC) line for pancreatic and duodenal homeobox 1 (PDX1) (PDX1:H2B-GFP, using histone 2B) and for neurogenin 3 (NEUROG3) (NEUROG3:tagRFP-T) to mark PPs and endocrine progenitors, respectively (Figures S1A–S1C). We have previously reported a method to differentiate hPSCs in 2-dimensions (2D) into PPs and expand them as organoids (PP organoids) in 3D that we adapted to 384-well plates (Figure S1D).[14] Following initial expansion for 3 days, these PP organoids were treated against a library of 538 annotated small molecules (Figure 1A; Table S1) encompassing compounds that are cell-permeable and annotated for inhibition of protein kinases or regulation of stem cell biology targeting a diverse set of known biological pathways (Table S1; STAR Methods). After 7 days of treatment, the PP organoids were fixed and stained for DAPI (as a nuclear marker) and phalloidin (an F-actin marker). Images were acquired with an automated spinning disc microscope for four channels (PDX1:H2B-GFP, NEUROG3:tag-RFP-T, DAPI, and phalloidin-AF647) and four planes in z at a distance of 10 μm (Figure 1A). Individual nuclei were segmented based on DAPI signals, whereas F-actin combined with DAPI was used to demarcate organoid boundaries. A set of 441 multivariate features for fluorescence intensity, radial intensity distributions, and shape was extracted for all four channels based on the segmented nuclei and organoids (Table S2). The primary screen was conducted on three independent experiments, generating about 1.38×10^5 images, including 603,902 profiled organoid objects and 19,883,057 nuclei. We set up 4 complementary analysis pipelines to data-mine the feature-rich dataset (as described in STAR Methods), leading up to the identification of 54 hit compounds. Prior to hit selection, we excluded 212 compounds with more than 30% reduction in cell number—possibly due to toxicity or effects on proliferation.

The first pipeline—referenced as "well-mean analysis" (Figure 1B)—aimed to find compounds changing the phenotypic profile based on well-averaged features, compared with the control treated with dimethyl sulfoxide (DMSO). The profiles were built based on a subset of features with low redundancy (see STAR Methods). Finally, 22 compounds were flagged as hits, as they showed reproducible feature profiles between biological replicates (Tables S1 and S2). Example hits from the well-mean analysis are shown in Figures 1C and S2A.

The second pipeline, binning analysis, tackled the problem of heterogeneous morphologies that PP organoids exhibited (Figure S1D). Using average measurements of organoid objects per well has a limited discriminating power to identify phenotypes due to this heterogeneity. This led us to perform a subpopulation analysis for features accounting for the shape and size of objects, fluorescence distribution, as well as the lumen presence and its size. The percentage of organoid in bins defined by low-, medium-, or high-value quantiles for each feature based on the control population (DMSO) was calculated, and these bin thresholds were applied to all objects treated with compounds. This revealed population shifts in experimental conditions (Figures 1D, 1E, and S2B). Binning analysis led to the identification of 43 hit compounds (Tables S1 and S2).

The focus of the third pipeline, network analysis, was to capture compounds changing the spatial arrangement of cells within organoids. For each organoid, we retrieved statistical features based on the network morphology built with the locations of nuclei as nodes and edges, calculated by applying a Delaunay triangulation[16] (Figure 1F; Tables S1 and S2). We retrieved 8 hits as exemplified in Figures 1G and S2C.

Both binning and network analysis pipelines do not use multiparametric profiles, because each feature was analyzed independently. Therefore, in a fourth analysis, namely morphological clustering, we used a clustering approach on a phenotypic fingerprint generated by a curated selection of features describing the morphology of each organoid. To determine clusters based on these fingerprints, we first reduced the high-dimensional dataset, including both control and experimental organoids, to 2D by applying the uniform manifold approximation and projection (UMAP) to overcome the curse of dimensionality.[17] A spectral clustering was then applied and split the projected dataset into several phenotypic clusters sharing similar fingerprints. The initial analysis of the entire dataset distinguished two main clusters: objects with lumen and objects without lumen. Then we further refined the analysis on each of these independent clusters—organoids with and without lumen. 22 compounds showing

(B and C) Flowchart of well-mean analysis. Features for nuclear and organoid measurements were averaged per well and compared with the DMSO-treated negative control. (C) An example hit from well-mean analysis shows CHIR treatment decreased the mean GFP intensity in organoids. $N = 3$. Data represented as mean ± SD. *****$p < 0.00001$.

(D and E) Binning analysis. Graphical representation of the binning analysis for a feature (D). The distribution for each feature of the DMSO control was divided into three bins of an equal number of objects, and the same binning thresholds were applied for the treatment conditions. z-factors for each bin were calculated to quantify the increase or decrease in the number of objects. An example hit (E) by Myriocin (*Mycelia sterilia*) treatment shows enriched objects with a smaller area compared with the control. $N = 3$. Data represented as mean ± SD. **$p = 0.0027$.

(F and G) Network analysis using the principle of Delaunay triangulation to build non-intersecting triangles. The nuclear arrangement inside an organoid was quantified by network analysis (F). An example hit (G) by Myriocin (*Mycelia sterilia*) treatment resulted in organoids with closely arranged nuclei with a lower distance (less than 35 pixels) between the neighbors. $N = 3$. Data represented as mean ± SD. *****$p < 0.00001$.

(H–J) Clustering of organoids in the morphospace. PP organoids with lumen from the primary screen are grouped into 6 clusters (H), and representative images of organoids are taken from the center of each cluster (I). Nuclei (DAPI) in gray, PDX1:H2B-GFP in green, and F-actin (phalloidin) in magenta. Scale bars, 30 μm. An example hit profile of GW1929 treatment shows enriched objects in cluster 1 (J).

(K) Overview of hits from the primary screen. A total of 54 hits were identified from the primary screen, and some hits were identified in multiple analyses.

See also Figures S1 and S2.

increased or decreased presence of organoids within such a cluster were flagged as hits (Tables S1 and S2). We visualized 6 clusters for the objects with lumen on the UMAP (Figures 1H and 1I) and 5 clusters for the objects without lumen (Figures S2D–S2F). For organoids with lumen, we observed distinct segregation based on the lumen morphology (Figure 1I). Clusters 0 and 1 consisted of organoids with concentrated apical actin, with cluster 1 having the highest intensity levels. Clusters 2, 3, and 4 had organoids with a single lumen, with cluster 2 being closer to cluster 1 and consisting of higher levels of apical actin. Cluster 3 consisted of organoids with mostly a monolayer of cells lining an enlarged lumen. Cluster 5 consisted of organoids with relatively smaller lumen size as well as relatively higher levels of actin on the basal side. The cluster enrichment of organoids is shown for an example hit in Figure 1J.

Using the four analysis pipelines outlined above collectively, we identified a total of 54 hits from the primary screen, 6 of which were identified by all four analysis pipelines (Figures 1K and S2G; Table S1). 11 compounds were selected for validation, prioritizing those identified by multiple analyses and the phenotypes observed (Table S1). For those, we performed dose-response validations with concentrations ranging from 0.1 to 10 μM (see examples in Figures 2F, 2G, and S3). It is worth noting that no compounds specifically affected the endocrine differentiation readout NEUROG3:tagRFP-T.

GSK3 inhibition increases lumen occupancy and decreases PDX1 expression in PP organoids

The targets with the most hits on the screen were GSK3α and β (GSK3A and GSK3B), two serine/threonine kinases involved in multiple biological pathways.[18,19] Six GSK3 inhibitors were identified as hits from multiple analysis pipelines (Figures 2A–2E; Table S1). Unlike the selective GSK3B inhibitors among the hits, CHIR99021 (CHIR), a widely used potent inhibitor of both GSK3A and GSK3B, displayed the strongest phenotype, exhibiting changes in cell identity as well as the organoid morphology, i.e., a decrease in PDX1-proxy GFP intensity and an increase in lumen occupancy, which is the ratio of lumen area to the total organoid area (Figures 2B, 2F, and 2G). Upon validation, CHIR was not toxic in the tested range of concentrations (Figure S3A), and its half-maximal inhibitory concentration (IC_{50}) for GFP+ nuclei was 1 μM (Figure 2F), whereas other inhibitors of both GSK3A and GSK3B, such as TWS119, had an effect closer to their toxic dose (Figures S3B–S3D). To quantify the effect on morphologies across different concentrations, we performed quantile binning analysis with five bins for morphological features. At concentrations of 1–3 μM, CHIR treatment significantly enriched organoids in bin 5 with larger lumens (Figure 2G). Additionally, morphological clustering was performed on the organoids treated with different dosages of compounds during validation experiments, and this time, 7 clusters were visualized for objects with lumen (Figure 2H). Organoids treated with CHIR at 3 μM were enriched in cluster 2, exhibiting enlarged lumen (Figures 2H and 2I), while at 0.1 μM they were distributed across all clusters (Figure 2H). These observations thus validated the morphological phenotype observed in the screen. Taken together, our experiments show that GSK3 activity regulates PP identity marked by PDX1 expression as well as the morphology of PP organoids.

GSK3 inhibition-induced phenotype is partially reversible upon removal of the compound

Using flow cytometry analysis to examine the expression of PP marker proteins, we confirmed a reduction of PDX1:H2B-GFP intensity as well as of PDX1 and NK-6 homeobox 1 (NKX6-1) expression after 7 days of CHIR treatment (referred to as CHIR-7days) on organoids derived from multiple hPSC lines (Figures 3A–3D). To test whether CHIR triggered a permanent loss of PP identity or a temporary effect during drug treatment, PP organoids were treated with CHIR for 4 days, i.e., from days 3 to 7, and then with culture medium with DMSO for the last 3 days until day 10 (Figure 3A). Hereafter, this treatment is referred to as CHIR-4days. Expression of PDX1:H2B-GFP, PDX1, as well as NKX6-1, was restored to control levels within 3 days of compound withdrawal in the CHIR-4days condition (Figures 3B–3D and S5A–S5E), which was confirmed with multiple cell lines. Imaging of the PP organoids also confirmed that the CHIR-4days samples exhibited decreased PDX1:H2B-GFP intensity and an enlarged lumen after 4 days of treatment at day 7. At day 10, after 3 days of withdrawal, these organoids had regained PDX1:H2B-GFP expression but still retained a single enlarged lumen (Figure 3E). Hence, we could rescue the cell identity phenotype of CHIR treatment by removing the compound from the culture medium, but not the morphological phenotype. This indicates that PPs maintain their cellular plasticity during temporary treatment of CHIR for 4 days, but the PP-organoid morphology is not as plastic as their gene expression. Moreover, while the reduction of PDX1 expression was reproducible across all cell lines, the lumen enlargement was confirmed in only 3 out of 5 lines.

To identify underlying biological pathways and mechanisms of the phenotypes induced by CHIR on PP organoids, we performed bulk RNA sequencing on the CHIR-treated organoids. To examine transcriptional profiles of the phenotypes observed in the screen, day 10 samples of CHIR-7days and CHIR-4days conditions, as well as DMSO control, were collected. Additionally, to investigate short-term responses, samples at day 4, i.e., 1 day after CHIR treatment (day 4 CHIR-1day), and DMSO control were also included (Figure 3F). Principal component analysis revealed that day 4 CHIR-1day and day 10 CHIR-7days clustered separately from the day 4 DMSO and day 10 DMSO, respectively (Figure 3G). However, day 10 CHIR-4days samples clustered closer to day 10 DMSO, whereas the day 10 CHIR-7days samples clearly segregated distantly from them (Figure 3G), supporting the observed results of the partial rescue of the phenotype upon withdrawal of CHIR (Figures 3B–3E).

Transcriptome analysis further supported the loss of PP markers by CHIR observed by live imaging and flow cytometry, showing a reduction of *PDX1* and *NKX6.-1* at days 4 and 10, along with PP markers such as one cut homeobox 1 (*ONECUT1*), HNF1 homeobox B (*HNF1B*), Gata binding protein 4 (*GATA4*), and nuclear receptor subfamily 5 group A member 2 (*NR5A2*) (Figure 3H). This effect, however, was not general, as other PP markers such as SRY-box transcription factor 9 (*SOX9*), Gata binding protein 6 (*GATA6*), TEA domain transcription factor 1 (*TEAD1*), and forkhead box A2 (*FOXA2*) remained unchanged.

Since a subset of PP markers was decreased by CHIR and was restored upon withdrawal of the compound, we investigated

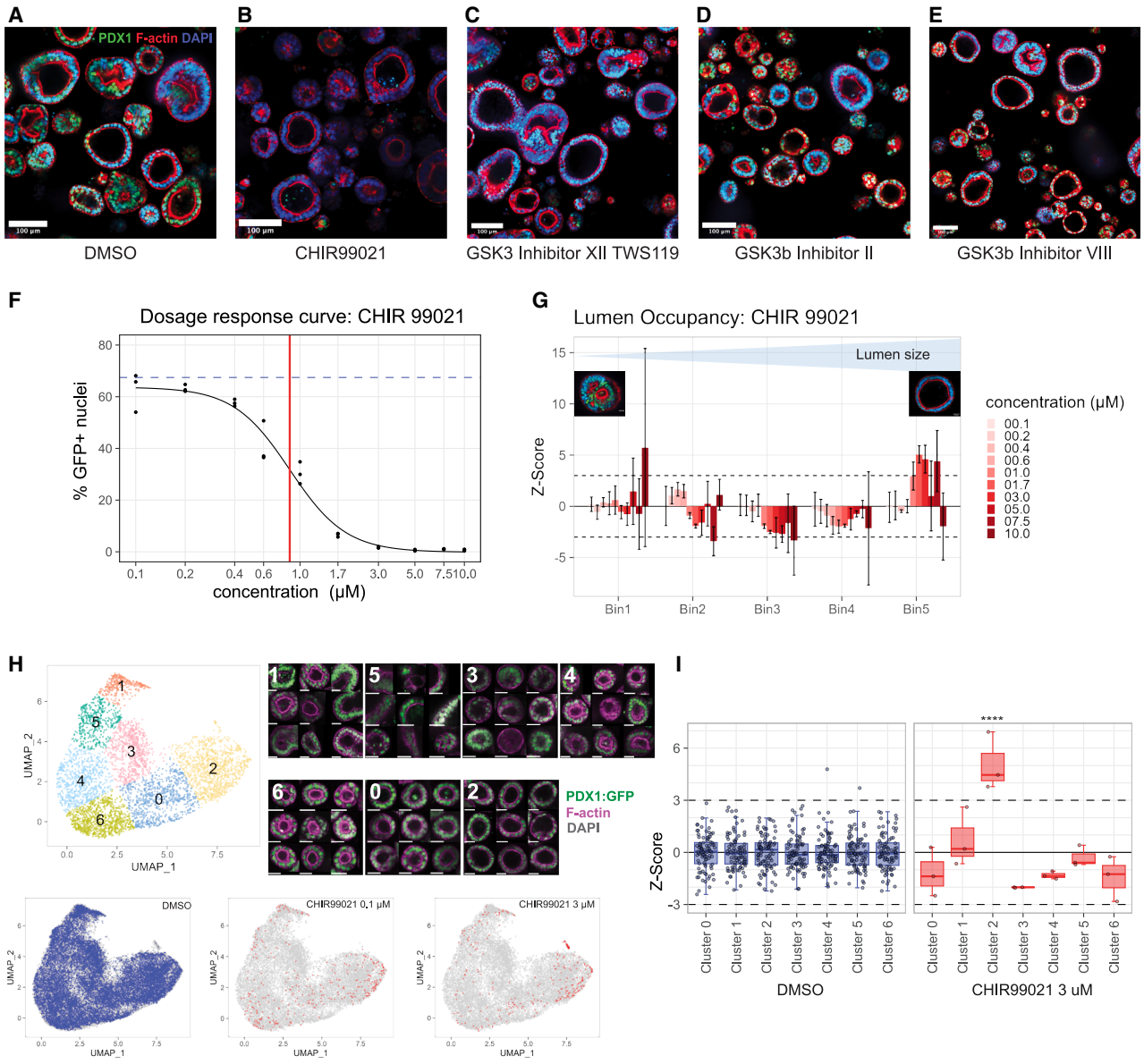

Figure 2. GSK3 inhibition reduces PDX1 expression and changes the morphology of PP organoids

(A–E) Representative images of wells treated with negative control DMSO (A) and 4 different GSK3 inhibitors (B–E) identified as hits from the primary screen. PDX1:H2B-GFP in green, nuclei (DAPI) in blue, and F-actin (phalloidin) in red. Scale bars, 100 μm.

(F) Dose-response curve showing the % GFP+ nuclei at different concentrations of CHIR. The dashed blue line represents the level of the DMSO control, and the red line denotes the IC_{50} concentration.

(G) Lumen occupancy quantified by binning analysis for CHIR at different concentrations. Bin 1 has the lowest lumen occupancy, corresponding to a smaller lumen size, whereas bin 5 has the highest lumen occupancy, corresponding to a bigger lumen size. *Z* score = |3| corresponds to $p = 0.012419$, and the higher the *Z* score, the lower the *p* value. Data represented as the mean of all wells with a given treatment ± SD.

(H and I) UMAP representation of the morphology clustering of all organoids with lumen, irrespective of their treatments, from the IC_{50} validation experiment (H). Each dot represents an organoid. Organoids corresponding to the center of each cluster are shown with the nucleus in gray, PDX1 in green, and F-actin in magenta. Organoids are scaled to the same size for representation. In DMSO and 0.1 μM CHIR conditions, organoids are distributed across all clusters, while in 3 μM CHIR, organoids are enriched in cluster 2 with a stronger phenotype, corresponding to objects with larger lumen (I). Scale bars: 30 μm in (H). In (I), data are represented as the mean of all wells with a given treatment ± SD.

See also Figure S3.

if a hallmark of PPs, namely their ability to differentiate into endocrine cells, was affected. To investigate their functionality, PP organoids treated with DMSO, CHIR-7days, or CHIR-4days were differentiated into pancreatic endocrine cells using the stage 5 and stage 6 media from the Rezania et al. protocol.[20,21] Analysis of stage 6 day 14 cells by flow cytometry showed no differences

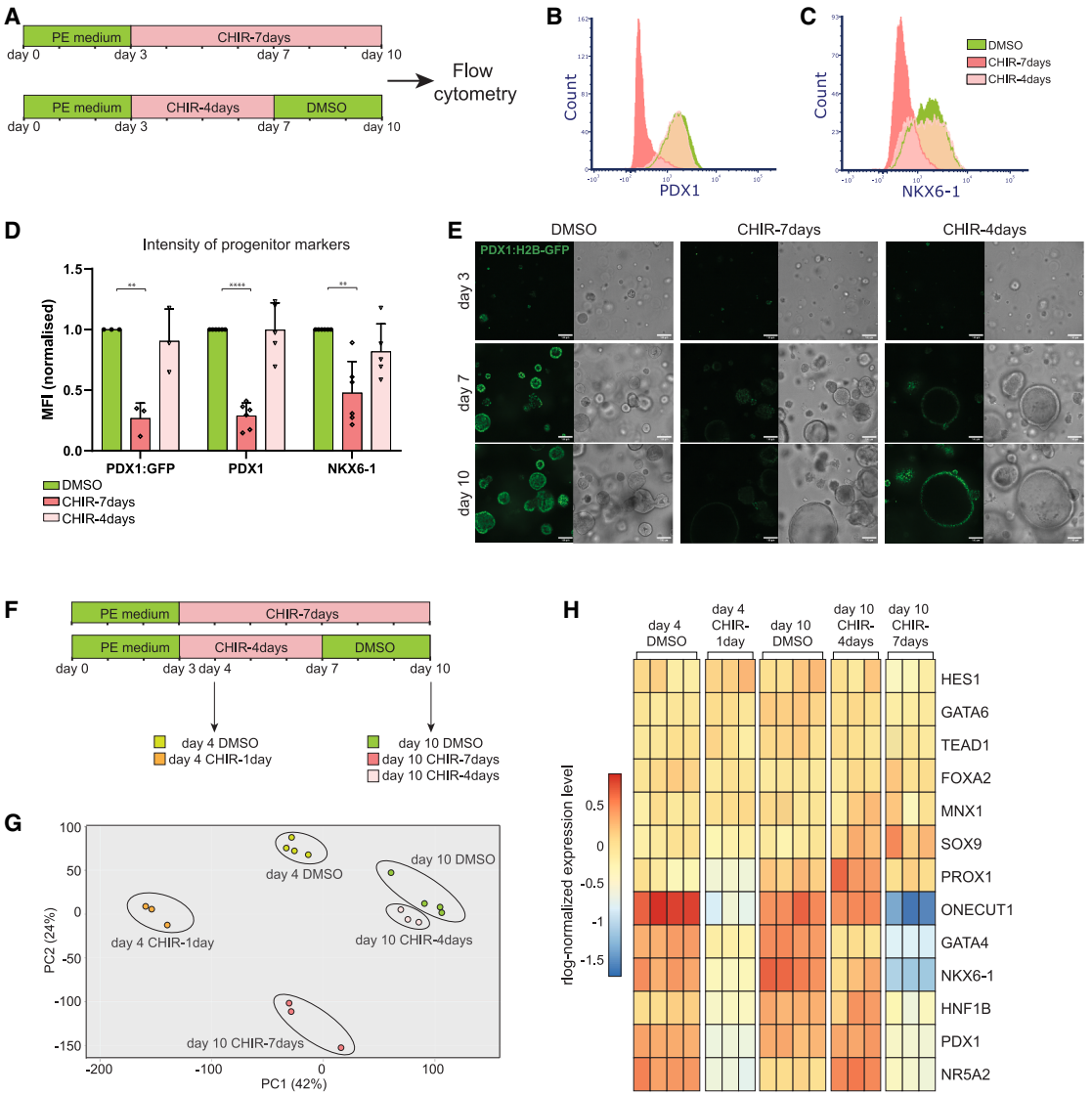

Figure 3. Effect of CHIR on PPs and partial rescue of the phenotype after withdrawal

(A) Schematic representation of experiment for CHIR treatments on PP organoids.

(B and C) Flow cytometry analysis for the expression of PP markers PDX1 (B) and NKX6-1 (C) of the day 10 PP organoids treated with CHIR ($N > 3$).

(D) Mean fluorescence intensity of the progenitor markers from flow cytometry normalized to the DMSO control. PDX1:H2B-GFP is the native GFP signal of the reporter ($N = 3$), while PDX1 and NKX6-1 ($N = 6$) are signals from antibodies used for the analysis of multiple cell lines. Data represented as mean ± SD. $^{****}p < 0.00001$, $^{**}p < 0.01$.

(E) Representative images of PP organoids acquired on days 3, 7, and 10. CHIR-7days organoids exhibit increased lumen size and decreased GFP signal compared with DMSO control on days 7 and 10. CHIR-4days organoids show decreased GFP intensity on day 7 but recovery of the GFP signal on day 10. Scale bars, 100 μm. PDX1:H2B-GFP in green.

(F) Schematic representation of experimental design for CHIR treatment on PP organoids for bulk RNA sequencing ($N = 3$).

(G) Principal component analysis plot of the CHIR-treated samples from the bulk RNA sequencing data.

(H) Heatmap showing centered rlog-normalized expression levels of PP markers after treatment with CHIR.

See also Figures S4 and S5.

in the percentage of c-peptide- and glucagon-expressing cells (Figure S4A). Importantly, the differentiation media do not contain CHIR, supporting the observation that progenitors largely revert to their original potency and functionality after CHIR removal. Keeping CHIR throughout the differentiation resulted in a severe loss of cell viability.

Canonical WNT signaling underlies the phenotype induced by GSK3 inhibition

In order to identify the biological pathways affected by CHIR treatment, we performed Gene Ontology (GO) term enrichment on the differentially expressed genes (DEGs) from the transcriptome. While the first categories indicated changes in cellular

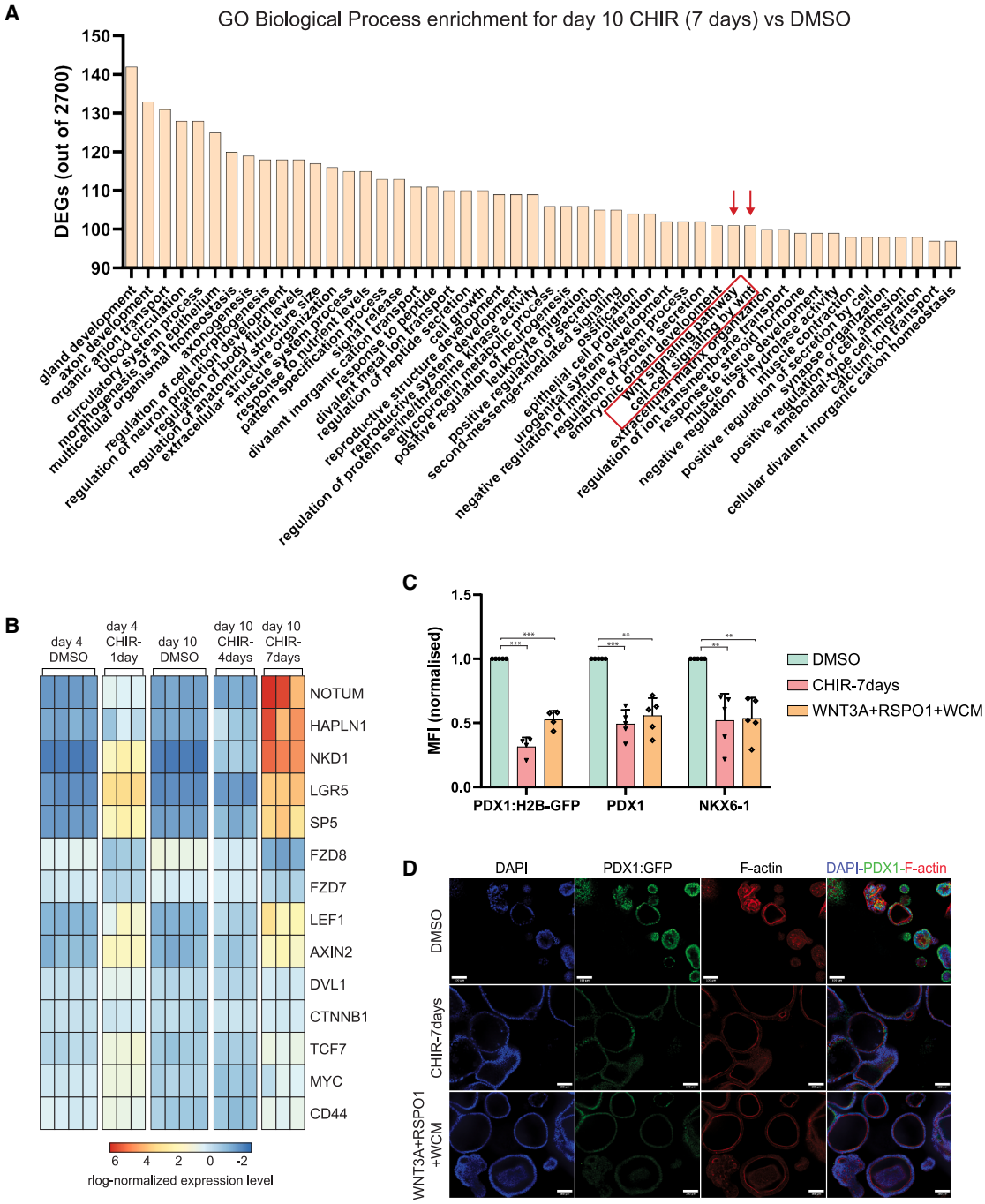

Figure 4. Canonical WNT activation reproduces the phenotypes induced by GSK3 inhibition

(A) GO term enrichment for day 10 CHIR-7days compared with day 10 DMSO. Red arrows indicate enriched WNT-related pathways.

(B) Heatmap showing centered rlog-normalized expression levels of selected canonical WNT candidate genes after CHIR treatment.

(C) Mean fluorescence intensity levels of PDX1:H2B-GFP, PDX1, and NKX6-1 analyzed by flow cytometry ($N = 5$). WCM, WNT-conditioned medium. Data represented as mean ± SD. ***$p < 0.001$, **$p < 0.01$.

(D) Representative images of PDX1:H2B-GFP PP organoids treated with DMSO, CHIR, and canonical WNT activation for 7 days and fixed on day 10. Scale bars, 100 μm. PDX1:H2B-GFP in green, F-actin in red, and DAPI in blue.

See also Figures S4 and S5.

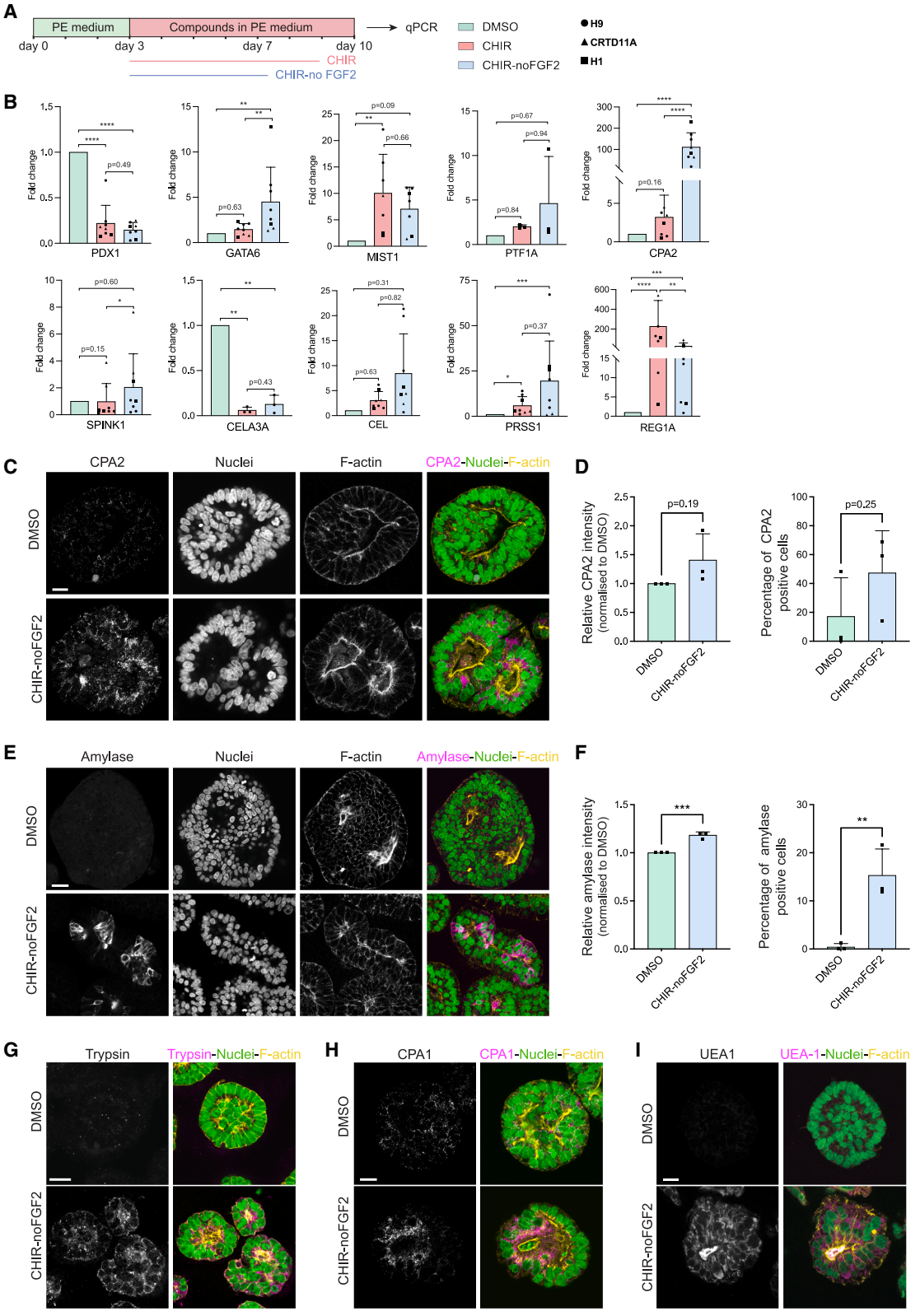

(legend on next page)

processes, including gland development, the first pathway highlighted was WNT signaling (Figure 4A). Identifying the most significantly changing genes in the transcriptome underlined the canonical WNT signaling, including the upregulation of leucine rich repeat containing G protein-coupled receptor 5 (*LGR5*), transcription factor 7 (*TCF7*), Axin 2 (*AXIN2*), NKD inhibitor of Wnt signaling pathway 1 (*NKD1*), notum, palmitoleoyl-protein carboxylesterase (*NOTUM*), and Sp5 transcription factor (*SP5*) in day 4 CHIR-1day and day 10 CHIR-7days samples (Figure 4B). Several WNT receptors, such as *FZ7* and *FZ8*, were downregulated, possibly due to negative feedback, which is suggested by the substantial increase of the dishevelled (DVL) negative regulator, *NKD1*.[22] However, little difference was observed in expression levels of these WNT genes between day 10 DMSO and day 10 CHIR-4days samples (Figure 4B), supporting again the rescue upon CHIR withdrawal (Figures 3D, 3E, and S5A–S5E). Another set of genes that were flagged by the DEGs were proliferation and cell cycle regulators. Upregulation of these genes was observed at day 4 CHIR-1day but not at day 10 CHIR-7days (Figure S4B), suggestive of a temporary proliferative effect in early phase upon CHIR treatment. Little difference was observed in the expression levels of proliferation markers between day 10 DMSO and day 10 CHIR-4days samples (Figure S4B). Based on this early, temporary proliferative signature and the lumen expansion observed upon temporary treatment of CHIR between days 4 and 7 (Figure 3E), it is possible that the lumen enlargement is due to an increased proliferation rate at early time points after CHIR treatment.

The results from transcriptomics suggested a role of the canonical WNT signaling in driving the phenotypes of CHIR treatments. To test this hypothesis, PP organoids were treated with WNT3A and RSPO1 proteins and a WNT-conditioned medium in different combinations (Figures 4C and S4C). Analysis by flow cytometry showed no effect on PP expression upon WNT3A and RSPO1 treatments, potentially due to a lower activity of purified recombinant proteins (Figure S4C). Nonetheless, upon supplementation with WNT-conditioned medium, a significant decrease in PDX1:H2B-GFP, PDX1, and NKX6-1 expression was confirmed (Figure 4C). The morphological phenotype of lumen enlargement was also reproduced after treatment with WNT3A and RSPO1 in WNT-conditioned medium (Figure 4D). Therefore, our results support that canonical WNT signaling may be responsible for the phenotypes induced by CHIR.

WNT activation in combination with inhibition of FGF signaling induces acinar differentiation of PP organoids

To investigate the biological relevance of the phenotypes observed, we considered three hypotheses. First, a decrease in PDX1 and other PP markers would be expected if the PPs were converted into liver, intestine, or stomach.[23–26] However, no significant increase was observed in marker expression of these organs from the transcriptomics and qPCR data (Figures S4D, S4F, and S4G). Secondly, differentiation of PPs into endocrine cells was also ruled out, as these organoids were not positive for the endocrine progenitor reporter NEUROG3:tag-RFP-T. A third hypothesis was the induction of acinar development, as a decrease in PDX1 expression is expected in the acinar lineage based on studies in mice.[27,28] In support of this hypothesis, our transcriptomics data suggested an upregulation of basic helix-loop-helix family member a15 (*BHLHA15*), the gene encoding MIST1 protein, a key transcription factor driving the pancreatic acinar cell differentiation program, along with the gene for digestive enzyme serine protease 2 (*PRSS2*), upon CHIR treatment (Figure S4E). This was confirmed by qPCR, which also revealed an upregulation of *BHLHA15* and the digestive enzyme genes carboxypeptidase A2 (*CPA2*) and serine protease 2 (*PRSS1*), encoding trypsinogen (Figure 5B). However, the fold increase was rather moderate (3- to 10-fold), even though it was similar to the levels reported in previous publications aiming at differentiating acinar cells.[29–31] Additionally, GO term enrichment highlighted genes involved in ion transport and peptide secretion but no other acinar markers (Figure 4A). We reasoned that even though acinar cells are first detected at embryonic day 14.5 (E14.5) in mice, the first acinar-committed cells emerge in mice at E11.5,[32] coinciding with the cessation of FGF10 production by the mesenchyme surrounding the pancreas epithelium.[33] Although these cells express carboxypeptidase A, it takes several days for other enzymes, such as amylase, to become detectable at E14.5. We therefore hypothesized that a decrease in FGF signaling may be important for acinar cell induction. To test this hypothesis, we treated PP organoids with different combinations of WNT activation via CHIR treatment and inhibition of FGF either by removal of FGF2 from the medium or addition of SU5402, an inhibitor of FGFR (Figures 5A and S6B). Gene expression analysis confirmed that treatment of CHIR along with FGF inhibition, either by removal of FGF2 or by addition of the FGFR inhibitor, increased the expression of acinar enzymes, such as *CPA2* by over 100-fold, *PRSS1* (about 20-fold), carboxyl ester lipase (*CEL*) (about 8.5-fold), transcription factors such as *BHLHA15/MIST1* (about 7-fold), and *GATA6* (about 4.5-fold), as well as other markers shown to be enriched in acinar cells, such as serine peptidase inhibitor Kazal type 1 (*SPINK1*) and regenerating family member 1 alpha (*REG1A*) (Figures 5B and S6C). However, another enzyme, *CELA3A*, was downregulated (Figure 5B), suggesting that the acinar cells are not fully mature.

Figure 5. Combination of WNT activation and FGF inhibition induces acinar differentiation in PP organoids

(A) Schematic representation of the experiment for acinar differentiation of PP organoids.

(B) Gene expression analysis by qPCR for PP and acinar markers across 3 hPSC lines ($N = 3–8$). Fold change indicates relative fold change normalized against DMSO control. Data represented as mean ± SD. $^{****}p < 0.0001$, $^{***}p < 0.001$, $^{**}p < 0.01$, $^{*}p < 0.05$.

(C, E, and G–I) Images of optical sections from whole-mount immunostained organoids for acinar markers. Concurrent CHIR treatment and FGF2 withdrawal from day 3 upregulate multiple acinar markers such as CPA2 (C), amylase (E), trypsin (G), CPA1 (H), and UEA1 (I). Nuclei (Hoechst 33342) and F-actin (phalloidin) staining are also shown in conditions. Scale bars, 20 μm. $N = 5$.

(D and F) Quantifications of the average intensity of CPA2 (D) and amylase (F) in organoids upon concurrent CHIR treatment and FGF2 withdrawal from days 3 to 10 relative to DMSO controls. Quantifications of the positive cell proportions with detectable CPA2 (D) and amylase (F). $N = 3$, with >10 organoids averaged per biological replicate. Data represented as mean ± SD. $^{***}p < 0.001$, $^{**}p < 0.01$.

See also Figures S6 and S7.

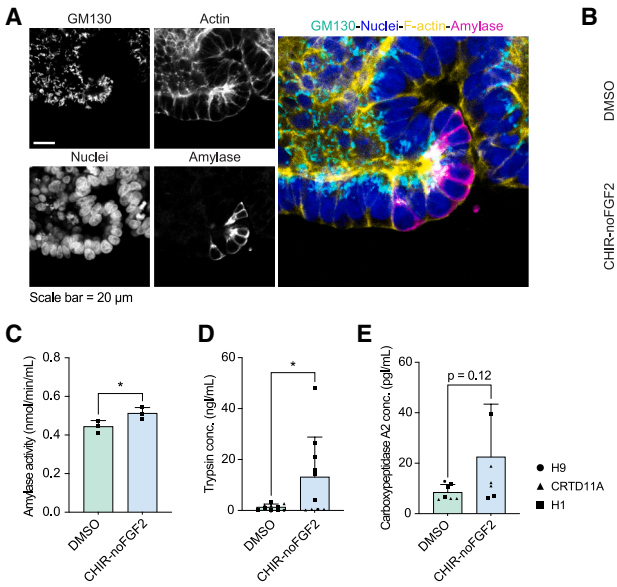

Figure 6. Combination of WNT activation and FGF inhibition induces acinar functional features

(A) Representative image of optical sections from whole-mount immunostained organoids in the CHIR + noFGF2 condition. A subset of cells expresses the acinar marker amylase with basal nuclei forming a bulging rosette-like acinar structure exhibiting apical constriction, rich in F-actin, and abundant apical Golgi marked by GM130. Scale bar, 20 μm.

(B) Images by transmission electron microscopy. CHIR + noFGF2-treated organoid contains cells with zymogen vesicles typically observed in the acinar cells. Scale bars, 10 μm. $N = 3$.

(C) Quantification of amylase activity measured in supernatants from organoids cultured in CHIR + noFGF2 and control DMSO conditions. $N = 3$. Data represented as mean ± SD. $^{*}p < 0.05$.

(D) Quantification of trypsin concentration in supernatants, measured by ELISA from organoids cultured in CHIR + noFGF2 and control DMSO conditions. $N = 10$. Data represented as mean ± SD. $^{*}p < 0.05$.

(E) Quantification of CPA2 concentration in supernatants, measured by ELISA from organoids cultured in CHIR + noFGF2 and control DMSO conditions. $N = 7$. Data represented as mean ± SD.

To further examine spatial expression and differentiation of acinar markers, we performed immunofluorescence staining focusing on the conditions with CHIR, with the removal of FGF2. Immunostaining indeed confirmed the formation of rosette-like acinar structures, with concentrated apical F-actin, ezrin, zonula occludens 1 (ZO-1), and atypical protein kinase C (aPKC), and larger nuclei at the basal side in organoids (Figures 5C, 5E, 5G–5I, and S7A–S7C). These rosette-like cells expressed acinar enzymes such as amylase, trypsin, CPA1, and CPA2, as well as being labeled with the acinar marker Ulex europaeus Agglutinin 1 (UEA-1)[34] (Figures 5C, 5E, 5G–5I, and S7A–S7D). Quantifications of images showed that while the average amylase and carboxypeptidase intensity was globally increased, the proportions of cells expressing enzymes were different, with an estimate of 15% cells for amylase and 40% cells for carboxypeptidase (Figures 5D and 5F). Notably, cells expressing high levels of SOX9 were devoid of enzymes (Figure S7D). Moreover, the enzyme-expressing cells exhibited an abundant apically positioned Golgi, as expected for an exocrine cell (Figure 6A). Additionally, electron microscopy images showed the presence of abundant zymogen vesicles (Figure 6B), a typical signature of pancreatic acinar cells. Moreover, we examined the functionality of exocrine cells, assessing enzyme secretion and activity. Upon carbachol stimulation, organoids treated with CHIR and no FGF2 exhibited significantly increased amylase activity, though to a modest level, and trypsin secretion by 15-fold, although an increase in CPA2 secretion was not statistically significant (Figures 6C–6E). We noted that there was rather a large variability across lines on these assays.

From the immunostainings, while carboxypeptidase staining seemed to be observed in many cells, the cells marked by amylase seemed more contrasted and yet more sparse, accompanied by distinctive proportions of cells expressing these enzymes (Figures 5C–5F). To further explore these proportions and obtain a more unbiased readout of the effect of CHIR and CHIR in the absence of FGF2, we conducted single-cell RNA sequencing on these conditions as compared with DMSO controls (Figures 7A–7C). This confirmed that acinar enzymes were induced in the conditions with CHIR and more so in CHIR without FGF2 (Figures 7B–7D, 7F, and 7K). Moreover, we observed that only a subpopulation of cells expressed *CPA1*, *CPA2*, *PRSS1*, *PRSS2*, *CEL*, and upregulated *GATA6* (Figures 7B–7D, 7F, and 7K). An unbiased assessment of GO categories enriched in each cluster also revealed an enrichment of genes in categories corresponding to zymogen, secretion, and digestion in cluster 1 containing mostly organoids grown with CHIR without FGF2 (Table S4). Moreover, we observed that these enzymes were not always co-expressed in the same cells. While this may be explained by the detection limits of the method, this may also be interpreted as a partial or unsynchronized acinar program being induced in each cell. We confirmed that progenitor and ductal/progenitor markers were also downregulated by CHIR (with and without FGF2) (Figures 7E, 7G, 7H, and 7K). A very small population of endocrine cells was found in all conditions (Figures 7I and 7K).

Taken together, the screen led us to identify multiple signaling molecules affecting human pancreas differentiation and morphogenesis in organoids in different ways. Particularly, concurrent activation of canonical WNT signaling and inhibition of FGF signaling are sufficient for inducing pancreatic acinar lineage differentiation as well as terminal acinus-like morphogenesis and function during human pancreas development.

DISCUSSION

In this study, we developed image-based high-content screening in the context of human organogenesis, challenged it with a library of small molecules, and established new readouts for morphological features by considering the innate heterogeneity in the organoids. Given the heterogeneity of many organoid

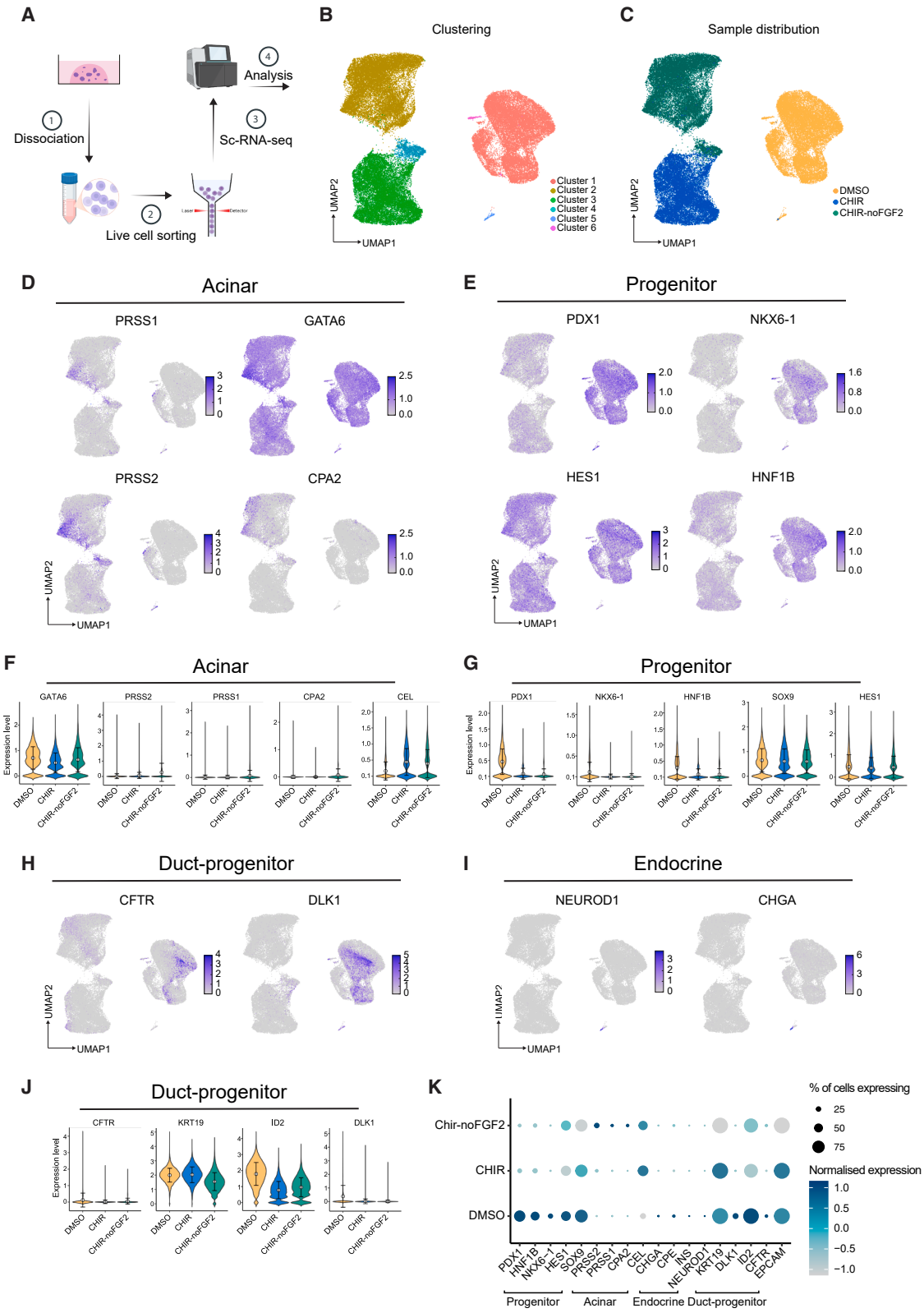

Figure 7. Single-cell transcriptome reveals efficient but partial production of acinar cells upon combined WNT activation and FGF inhibition

(A) Experimental workflow of the single-cell RNA sequencing experiments.

(B) UMAP representation of clustering of the single-cell samples into 6 clusters.

(legend continued on next page)

systems, we demonstrate that researchers should not hesitate to conduct screenings. Robust analytical methodologies can effectively handle this variability, identifying valuable biological information. In addition to the object morphology, our assay included proxies for a PP marker and an endocrine progenitor marker, thereby giving a readout for cell fate. Though the classical well-mean analysis pipeline identified some hits, we show that a subpopulation binning analysis is a critical tool to reveal hits in a heterogeneous population of objects for a given feature. In addition, we show that morphological clustering can classify different populations of organoids and identify how certain small molecules skew their distribution. Furthermore, network analysis quantifies nuclear arrangements inside organoids, providing morphological features of individual objects. Overall, our multi-modal assay exploits the potential of high-content analysis to explore cell identity as well as organoid morphology and could be applied to all features of interest in any organoid model system. Furthermore, our assay may be extended to CRISPR-based genetic screens to screen for morphological features beyond pooled genetic screening by sequencing.

Among the numerous hits identified in the screen, we show one example where the screen led to a biological discovery. Through GSK3 inhibition, we identified canonical WNT signaling as a modulator of PP identity as well as morphogenesis. CHIR, an inhibitor of GSK3A as well as GSK3B, showed the strongest phenotype among all the GSK3 inhibitors tested, suggesting that GSK3A and GSK3B may be functionally redundant for canonical WNT signaling in the pancreas, similar to what has been reported in mouse ESCs.[35] Studies from model organisms have shown that canonical WNT signaling is important at multiple stages of pancreas development. Its inhibition is critical for pancreas specification from the posterior foregut,[36–38] a process that is already completed in our human PP-organoid cultures when we add CHIR.[39] Following pancreas specification, activation of WNT is essential for progenitor expansion in mice,[40–44] which process is elicited in our human organoids through the presence of FGF,[14] another known cytokine promoting mouse PP proliferation.[33] The role of canonical WNT signaling on differentiation has been controversial but greatly clarified by Baumgartner et al.,[45] who showed that inhibition of beta-catenin reduces the formation of pro-acinar tip progenitors and thereby has secondary effects on acinar and beta cells.[40,41,43,45] It may also have an inhibitory effect on the endocrine lineage.[46–48] It was previously shown in mice that beta-catenin activation reduces the number of PDX1-positive cells and that its inhibition increases PDX1 in the duodenum,[42] suggesting that there is a conserved pathway by which WNT signaling via GSK3B and beta-catenin regulates PDX1. Here, we show that active WNT signaling in human PPs regulates the expression of many more progenitor markers, though not all of them, and promotes acinar precursor markers such as CPA2. We also show that WNT/CHIR do not trigger a transition but need to continuously signal to maintain this state, as the removal of CHIR partially reversed the phenotype, suggesting a plasticity of this cell state. By triggering differentiation in this state in the absence of CHIR, we show that the cells are still progenitors endowed with the ability to give rise to endocrine and acinar cells, like the tip cells in mice.[49]

We have previously shown that FGF signaling is essential for expansion of the progenitor pool during human pancreas development.[14] Here, we demonstrate that in addition to WNT activation, removal of FGF signaling allows the multipotent PPs to progress to acinar fate. Studies in mice have shown that the level of FGF10 decreases drastically from E11.5, coinciding with the initiation of acinar differentiation.[33,50–52] While previous studies have reported the initiation of acinar differentiation of hPSC-derived organoids,[15,29–31] our method induces more mature cells based on the levels of acinar marker expression, variety of markers observed, abundance of zymogen granules, and cellular organization into acini. *In vivo*, acinar enzymes in acinar cells reach 100- or 1,000-fold levels detected in progenitors or other cell types, in a gradual way.[53] Previously reported enrichments were in the order of 2- to 10-fold in those organoids,[15,29–31] while our organoid acinar differentiation reaches 10- to 100-fold increases. Moreover, the medium composition we use is extremely simple, thereby providing a useful tool to model exocrine pancreas and acinar pathologies in humans. Since acinar cells are thought to be the cell of origin of a majority of pancreatic adenocarcinoma, this provides an easily accessible PSC-derived model to study the initiation of adenocarcinoma.[54,55]

Limitations of the study

The organoid system used to conduct the screen recapitulates some aspects of pancreatic development. This includes the differentiation of progenitors into endocrine and exocrine cells, as well as some aspects of morphogenesis, notably cell polarization, acinar cell bulging, and rosette formation, but not all aspects, notably elongated tube formation and branching. Accordingly, we identified compounds affecting polarization, apical marker enrichment, ductal diameter, and epithelial thickness, which can be relevant to development. Other aspects relevant to development, which may have been observable, were not seen, such as increased endocrine differentiation and partial epithelial-mesenchymal transition (EMT). No compound affecting endocrine cells was identified, likely because the screening conditions were not poised enough for differentiation into endocrine cells. The conditions used respond efficiently to potent differentiation cocktails[14] but had a moderate response to single compounds

(C) Annotation of the three treatment conditions on the UMAP shown in (B).
(D) Acinar marker enrichment upon CHIR and further enrichment upon CHIR + noFGF2.
(E) Progenitor marker global repression (*PDX1*, *NKX6-1*, and *HNF1B*) upon CHIR and CHIR + noFGF2 treatment. No effect on hes family bHLH transcription factor 1 (*HES1*). Reduced *HES1* in cluster 3 upon CHIR and CHIR + noFGF2 treatment.
(F, G, and J) Violin plot showing the expression of specific marker expression in the 3 conditions, focusing on acinar (F), progenitor (G), and ductal/progenitor (J) markers.
(H) Ductal/progenitor marker repression upon CHIR and CHIR + noFGF2 treatment.
(I) Gene expression in the endocrine cluster comprising cells from all conditions.
(K) Quantitative dot plot representation of enrichment of specific markers across conditions.

such as known inducers of endocrine differentiation acting as gamma secretase inhibitors (XX or DAPT), especially in the 384-well format. Further important improvements envisioned for the future will be a more homogeneous induction of acinar cells and further maturity. This may be favored in more complex organoids, including mesenchyme.[56]

RESOURCE AVAILABILITY

Lead contact

Correspondence and requests for materials should be addressed to the lead contact, Anne Grapin-Botton (botton@mpi-cbg.de).

Materials availability

The hPSC line generated in this study is available from the lead contact upon request under a material transfer agreement.

Data and code availability

- Bulk RNA sequencing data of PP organoids treated with CHIR and control (DMSO) conditions is available in ArrayExpress: accession number: ArrayExpress: E-MTAB-14625.
- Single-cell RNA sequencing data of PP organoids grown in expansion conditions in the presence of DMSO (control) compared with those exposed for 7 days to CHIR or CHIR in the absence of the FGF2 normally included in the expansion medium is available in ArrayExpress: accession number: ArrayExpress: E-MTAB-16105.
- The code used for organoid image analysis in this study has been deposited in Zenodo and is available at https://doi.org/10.5281/zenodo.17854343.
- Additional information is available from the lead contact upon request.

ACKNOWLEDGMENTS

We acknowledge the support of the MPI-CBG facilities: Technology Development Studio, Organoid and Stem Cell Facility, FACS and Cell Technologies, Light Microscopy, Electron Microscopy, Scientific Computing Facility, Computer Department, and the Media Kitchen. We are grateful to Andre Gohr for the transcriptome analyses and to the Dresden Concept Genome Center for sequencing. We thank the Huch lab (MPI-CBG) for providing WNT-conditioned medium, Anthony Vega for help with organoid image analysis, Jana Meissner for help with TEM, Marit Leuschner and Jifeng Liu for help with cell line maintenance, and Allison Lewis and all members of the Grapin-Botton lab for engaging discussions.

Our work was funded by the Max Planck Society. R.K. was supported by the Deutsche Forschungsgemeinschaft (DFG, German Research Foundation) (project 288034826-IRTG 2251 to A.G.-B.).

AUTHOR CONTRIBUTIONS

R.K., M.B., M.S., R.B., Y.H.K., and A.G.-B. designed the screen. R.K., C.A., M.S., and R.B. performed the screen. A.J., R.K., M.S., and R.B. analyzed the screen. R.K., C.A., and K.K. performed the screen validation and/or mechanistic investigations. K.K. and R.K. conducted the characterization of acinar cell differentiation. R.K., K.K., Y.H.K., and A.G.-B. wrote the manuscript with input from A.J. All authors provided feedback on the manuscript.

DECLARATION OF INTERESTS

R.K., Y.H.K., K.K., and A.G.-B. are inventors on patent application EP24212058.2. M.B. was an employee of Roche at the time of the first submission. R.K. became an employee of Roche when revisions were submitted.

STAR★METHODS

Detailed methods are provided in the online version of this paper and include the following:

SUPPLEMENTAL INFORMATION

Supplemental information can be found online at https://doi.org/10.1016/j.stem.2025.12.023.

Received: December 7, 2024
Revised: October 21, 2025
Accepted: December 23, 2025
Published: January 21, 2026

REFERENCES

1. Grapin-Botton, A., and Kim, Y.H. (2022). Pancreas organoid models of development and regeneration. Development *149*, dev201004. https://doi.org/10.1242/dev.201004.
2. Zhao, Z., Chen, X., Dowbaj, A.M., Sljukic, A., Bratlie, K., Lin, L., Fong, E.L.S., Balachander, G.M., Chen, Z., Soragni, A., et al. (2022). Organoids. Nat. Rev. Methods Primers *2*, 94. https://doi.org/10.1038/s43586-022-00174-y.
3. Lewis, A., Keshara, R., Kim, Y.H., and Grapin-Botton, A. (2021). Self-organization of organoids from endoderm-derived cells. J. Mol. Med. (Berl.) *99*, 449–462. https://doi.org/10.1007/s00109-020-02010-w.
4. Corsini, N.S., and Knoblich, J.A. (2022). Human organoids: New strategies and methods for analyzing human development and disease. Cell *185*, 2756–2769. https://doi.org/10.1016/j.cell.2022.06.051.
5. Ungricht, R., Guibbal, L., Lasbennes, M.C., Orsini, V., Beibel, M., Waldt, A., Cuttat, R., Carbone, W., Basler, A., Roma, G., et al. (2022). Genome-wide screening in human kidney organoids identifies developmental and disease-related aspects of nephrogenesis. Cell Stem Cell *29*, 160–175.e7. https://doi.org/10.1016/j.stem.2021.11.001.
6. Ringel, T., Frey, N., Ringnalda, F., Janjuha, S., Cherkaoui, S., Butz, S., Srivatsa, S., Pirkl, M., Russo, G., Villiger, L., et al. (2020). Genome-Scale CRISPR Screening in Human Intestinal Organoids Identifies Drivers of TGF-β Resistance. Cell Stem Cell *26*, 431–440.e8. https://doi.org/10.1016/j.stem.2020.02.007.
7. Lampart, F.L., Iber, D., and Doumpas, N. (2023). Organoids in high throughput and high-content screenings. Front. Chem. Eng. *5*, 1120348. https://doi.org/10.3389/fceng.2023.1120348.
8. Lukonin, I., Serra, D., Challet Meylan, L., Volkmann, K., Baaten, J., Zhao, R., Meeusen, S., Colman, K., Maurer, F., Stadler, M.B., et al. (2020).

Phenotypic landscape of intestinal organoid regeneration. Nature *586*, 275–280. https://doi.org/10.1038/s41586-020-2776-9.

9. Lukonin, I., Zinner, M., and Liberali, P. (2021). Organoids in image-based phenotypic chemical screens. Exp. Mol. Med. *53*, 1495–1502. https://doi.org/10.1038/s12276-021-00641-8.

10. Suppinger, S., Zinner, M., Aizarani, N., Lukonin, I., Ortiz, R., Azzi, C., Stadler, M.B., Vianello, S., Palla, G., Kohler, H., et al. (2023). Multimodal characterization of murine gastruloid development. Cell Stem Cell *30*, 867–884.e11. https://doi.org/10.1016/j.stem.2023.04.018.

11. Mead, B.E., Hattori, K., Levy, L., Imada, S., Goto, N., Vukovic, M., Sze, D., Kummerlowe, C., Matute, J.D., Duan, J., et al. (2022). Screening for modulators of the cellular composition of gut epithelia via organoid models of intestinal stem cell differentiation. Nat. Biomed. Eng. *6*, 476–494. https://doi.org/10.1038/s41551-022-00863-9.

12. Keshara, R., Kim, Y.H., and Grapin-Botton, A. (2022). Organoid Imaging: Seeing Development and Function. Annu. Rev. Cell Dev. Biol. *38*, 447–466. https://doi.org/10.1146/annurev-cellbio-120320-035146.

13. Jennings, R.E., Berry, A.A., Strutt, J.P., Gerrard, D.T., and Hanley, N.A. (2015). Human pancreas development. Development *142*, 3126–3137. https://doi.org/10.1242/dev.120063.

14. Gonçalves, C.A., Larsen, M., Jung, S., Stratmann, J., Nakamura, A., Leuschner, M., Hersemann, L., Keshara, R., Perlman, S., Lundvall, L., et al. (2021). A 3D system to model human pancreas development and its reference single-cell transcriptome atlas identify signaling pathways required for progenitor expansion. Nat. Commun. *12*, 3144. https://doi.org/10.1038/s41467-021-23295-6.

15. Hohwieler, M., Illing, A., Hermann, P.C., Mayer, T., Stockmann, M., Perkhofer, L., Eiseler, T., Antony, J.S., Müller, M., Renz, S., et al. (2017). Human pluripotent stem cell-derived acinar/ductal organoids generate human pancreas upon orthotopic transplantation and allow disease modelling. Gut *66*, 473–486. https://doi.org/10.1136/gutjnl-2016-312423.

16. Delaunay, B. (1934). Sur la sphère vide. A la mémoire de Georges Voronoï. Известия Российской академии наук. Серия математическая *6*, 793–800.

17. McInnes, L., Healy, J., and Melville, J. (2018). Umap: Uniform manifold approximation and projection for dimension reduction. J. Open Source Softw. *3*, 861.

18. Beurel, E., Grieco, S.F., and Jope, R.S. (2015). Glycogen synthase kinase-3 (GSK3): regulation, actions, and diseases. Pharmacol. Ther. *148*, 114–131. https://doi.org/10.1016/j.pharmthera.2014.11.016.

19. Cohen, P., and Frame, S. (2001). The renaissance of GSK3. Nat. Rev. Mol. Cell Biol. *2*, 769–776. https://doi.org/10.1038/35096075.

20. Rezania, A., Bruin, J.E., Arora, P., Rubin, A., Batushansky, I., Asadi, A., O'Dwyer, S., Quiskamp, N., Mojibian, M., Albrecht, T., et al. (2014). Reversal of diabetes with insulin-producing cells derived in vitro from human pluripotent stem cells. Nat. Biotechnol. *32*, 1121–1133. https://doi.org/10.1038/nbt.3033.

21. Petersen, M.B.K., Azad, A., Ingvorsen, C., Hess, K., Hansson, M., Grapin-Botton, A., and Honoré, C. (2017). Single-Cell Gene Expression Analysis of a Human ESC Model of Pancreatic Endocrine Development Reveals Different Paths to beta-Cell Differentiation. Stem Cell Rep. *9*, 1246–1261. https://doi.org/10.1016/j.stemcr.2017.08.009.

22. Larraguibel, J., Weiss, A.R.E., Pasula, D.J., Dhaliwal, R.S., Kondra, R., and Van Raay, T.J. (2015). Wnt ligand-dependent activation of the negative feedback regulator Nkd1. Mol. Biol. Cell *26*, 2375–2384. https://doi.org/10.1091/mbc.E14-12-1648.

23. Offield, M.F., Jetton, T.L., Labosky, P.A., Ray, M., Stein, R.W., Magnuson, M.A., Hogan, B.L.M., and Wright, C.V.E. (1996). PDX-1 is required for pancreatic outgrowth and differentiation of the rostral duodenum. Development *122*, 983–995. https://doi.org/10.1242/dev.122.3.983.

24. Horb, M.E., Shen, C.N., Tosh, D., and Slack, J.M.W. (2003). Experimental conversion of liver to pancreas. Curr. Biol. *13*, 105–115. https://doi.org/10.1016/S0960-9822(02)01434-3.

25. Shen, C.N., Horb, M.E., Slack, J.M.W., and Tosh, D. (2003). Transdifferentiation of pancreas to liver. Mech. Dev. *120*, 107–116. https://doi.org/10.1016/S0925-4773(02)00337-4.

26. Fujitani, Y., Fujitani, S., Boyer, D.F., Gannon, M., Kawaguchi, Y., Ray, M., Shiota, M., Stein, R.W., Magnuson, M.A., and Wright, C.V.E. (2006). Targeted deletion of a cis-regulatory region reveals differential gene dosage requirements for Pdx1 in foregut organ differentiation and pancreas formation. Genes Dev. *20*, 253–266. https://doi.org/10.1101/gad.1360106.

27. Miyatsuka, T., Kaneto, H., Shiraiwa, T., Matsuoka, T.A., Yamamoto, K., Kato, K., Nakamura, Y., Akira, S., Takeda, K., Kajimoto, Y., et al. (2006). Persistent expression of PDX-1 in the pancreas causes acinar-to-ductal metaplasia through Stat3 activation. Genes Dev. *20*, 1435–1440. https://doi.org/10.1101/gad.1412806.

28. Ebrahim, N., Shakirova, K., and Dashinimaev, E. (2022). PDX1 is the cornerstone of pancreatic β-cell functions and identity. Front. Mol. Biosci. *9*, 1091757. https://doi.org/10.3389/fmolb.2022.1091757.

29. Merz, S., Breunig, M., Melzer, M.K., Heller, S., Wiedenmann, S., Seufferlein, T., Meier, M., Krüger, J., Mulaw, M.A., Hohwieler, M., et al. (2023). Single-cell profiling of GP2-enriched pancreatic progenitors to simultaneously create acinar, ductal, and endocrine organoids. Theranostics *13*, 1949–1973. https://doi.org/10.7150/thno.78323.

30. Huang, L., Holtzinger, A., Jagan, I., BeGora, M., Lohse, I., Ngai, N., Nostro, C., Wang, R., Muthuswamy, L.B., Crawford, H.C., et al. (2015). Ductal pancreatic cancer modeling and drug screening using human pluripotent stem cell- and patient-derived tumor organoids. Nat. Med. *21*, 1364–1371. https://doi.org/10.1038/nm.3973.

31. Huang, L., Desai, R., Conrad, D.N., Leite, N.C., Akshinthala, D., Lim, C.M., Gonzalez, R., Muthuswamy, L.B., Gartner, Z., and Muthuswamy, S.K. (2021). Commitment and oncogene-induced plasticity of human stem cell-derived pancreatic acinar and ductal organoids. Cell Stem Cell *28*, 1090–1104.e6. https://doi.org/10.1016/j.stem.2021.03.022.

32. Larsen, H.L., Martín-Coll, L., Nielsen, A.V., Wright, C.V.E., Trusina, A., Kim, Y.H., and Grapin-Botton, A. (2017). Stochastic priming and spatial cues orchestrate heterogeneous clonal contribution to mouse pancreas organogenesis. Nat. Commun. *8*, 605. https://doi.org/10.1038/s41467-017-00258-4.

33. Bhushan, A., Itoh, N., Kato, S., Thiery, J.P., Czernichow, P., Bellusci, S., and Scharfmann, R. (2001). Fgf10 is essential for maintaining the proliferative capacity of epithelial progenitor cells during early pancreatic organogenesis. Development *128*, 5109–5117. https://doi.org/10.1242/dev.128.24.5109.

34. Baldan, J., Houbracken, I., Rooman, I., and Bouwens, L. (2019). Adult human pancreatic acinar cells dedifferentiate into an embryonic progenitor-like state in 3D suspension culture. Sci. Rep. *9*, 4040. https://doi.org/10.1038/s41598-019-40481-1.

35. Doble, B.W., Patel, S., Wood, G.A., Kockeritz, L.K., and Woodgett, J.R. (2007). Functional redundancy of GSK-3alpha and GSK-3beta in Wnt/beta-catenin signaling shown by using an allelic series of embryonic stem cell lines. Dev. Cell *12*, 957–971. https://doi.org/10.1016/j.devcel.2007.04.001.

36. Heller, R.S., Dichmann, D.S., Jensen, J., Miller, C., Wong, G., Madsen, O.D., and Serup, P. (2002). Expression patterns of Wnts, Frizzleds, sFRPs, and misexpression in transgenic mice suggesting a role for Wnts in pancreas and foregut pattern formation. Dev. Dyn. *225*, 260–270. https://doi.org/10.1002/dvdy.10157.

37. Mclin, V.A., Rankin, S.A., and Zorn, A.M. (2007). Repression of Wnt/β-catenin signaling in the anterior endoderm is essential for liver and pancreas development. Development *134*, 2207–2217. https://doi.org/10.1242/dev.001230.

38. Nadauld, L.D., Sandoval, I.T., Chidester, S., Yost, H.J., and Jones, D.A. (2004). Adenomatous polyposis coli control of retinoic acid biosynthesis is critical for zebrafish intestinal development and differentiation. J. Biol. Chem. *279*, 51581–51589. https://doi.org/10.1074/jbc.M408830200.

39. Funa, N.S., Mjoseng, H.K., de Lichtenberg, K.H., Raineri, S., Esen, D., Egeskov-Madsen, A.R., Quaranta, R., Jørgensen, M.C., Hansen, M.S.,

van Cuyl Kuylenstierna, J., et al. (2024). TGF-beta modulates cell fate in human ES cell-derived foregut endoderm by inhibiting Wnt and BMP signaling. Stem Cell Rep. *19*, 973–992. https://doi.org/10.1016/j.stemcr.2024.05.010.

40. Murtaugh, L.C., Law, A.C., Dor, Y., and Melton, D.A. (2005). Beta-catenin is essential for pancreatic acinar but not islet development. Development *132*, 4663–4674. https://doi.org/10.1242/dev.02063.

41. Dessimoz, J., Bonnard, C., Huelsken, J., and Grapin-Botton, A. (2005). Pancreas-specific deletion of β-catenin reveals Wnt-dependent and Wnt-independent functions during development. Curr. Biol. *15*, 1677–1683. https://doi.org/10.1016/j.cub.2005.08.037.

42. Heiser, P.W., Lau, J., Taketo, M.M., Herrera, P.L., and Hebrok, M. (2006). Stabilization of β-catenin impacts pancreas growth. Development *133*, 2023–2032. https://doi.org/10.1242/dev.02366.

43. Wells, J.M., Esni, F., Boivin, G.P., Aronow, B.J., Stuart, W., Combs, C., Sklenka, A., Leach, S.D., and Lowy, A.M. (2007). Wnt/β-catenin signaling is required for development of the exocrine pancreas. BMC Dev. Biol. *7*, 4. https://doi.org/10.1186/1471-213x-7-4.

44. Papadopoulou, S., and Edlund, H. (2005). Attenuated Wnt signaling perturbs pancreatic growth but not pancreatic function. Diabetes *54*, 2844–2851. https://doi.org/10.2337/diabetes.54.10.2844.

45. Baumgartner, B.K., Cash, G., Hansen, H., Ostler, S., and Murtaugh, L.C. (2014). Distinct requirements for beta-catenin in pancreatic epithelial growth and patterning. Dev. Biol. *391*, 89–98. https://doi.org/10.1016/j.ydbio.2014.03.019.

46. Pedersen, A.H., and Heller, R.S. (2005). A possible role for the canonical Wnt pathway in endocrine cell development in chicks. Biochem. Biophys. Res. Commun. *333*, 961–968. https://doi.org/10.1016/j.bbrc.2005.05.189.

47. Scheibner, K., Bakhti, M., Bastidas-Ponce, A., and Lickert, H. (2019). Wnt signaling: implications in endoderm development and pancreas organogenesis. Curr. Opin. Cell Biol. *61*, 48–55. https://doi.org/10.1016/j.ceb.2019.07.002.

48. Sharon, N., Vanderhooft, J., Straubhaar, J., Mueller, J., Chawla, R., Zhou, Q., Engquist, E.N., Trapnell, C., Gifford, D.K., and Melton, D.A. (2019). Wnt Signaling Separates the Progenitor and Endocrine Compartments during Pancreas Development. Cell Rep. *27*, 2281–2291.e5. https://doi.org/10.1016/j.celrep.2019.04.083.

49. Zhou, Q., Law, A.C., Rajagopal, J., Anderson, W.J., Gray, P.A., and Melton, D.A. (2007). A multipotent progenitor domain guides pancreatic organogenesis. Dev. Cell *13*, 103–114. https://doi.org/10.1016/j.devcel.2007.06.001.

50. Elghazi, L., Cras-Méneur, C., Czernichow, P., and Scharfmann, R. (2002). Role for FGFR2IIIb-mediated signals in controlling pancreatic endocrine progenitor cell proliferation. Proc. Natl. Acad. Sci. USA *99*, 3884–3889. https://doi.org/10.1073/pnas.062321799.

51. Greggio, C., De Franceschi, F., Figueiredo-Larsen, M., Gobaa, S., Ranga, A., Semb, H., Lutolf, M., and Grapin-Botton, A. (2013). Artificial three-dimensional niches deconstruct pancreas development in vitro. Development *140*, 4452–4462. https://doi.org/10.1242/dev.096628.

52. Kobberup, S., Schmerr, M., Dang, M.L., Nyeng, P., Jensen, J.N., MacDonald, R.J., and Jensen, J. (2010). Conditional control of the differentiation competence of pancreatic endocrine and ductal cells by Fgf10. Mech. Dev. *127*, 220–234. https://doi.org/10.1016/j.mod.2009.11.005.

53. Han, J.H.R., Rall, L., and Rutter, W.J. (1986). Selective expression of rat pancreatic genes during embryonic development. Proc. Natl. Acad. Sci. USA *83*, 110–114. https://doi.org/10.1073/pnas.83.1.110.

54. Houbracken, I., de Waele, E., Lardon, J., Ling, Z., Heimberg, H., Rooman, I., and Bouwens, L. (2011). Lineage tracing evidence for transdifferentiation of acinar to duct cells and plasticity of human pancreas. Gastroenterology *141*, 731–741. 741.e1–4. https://doi.org/10.1053/j.gastro.2011.04.050.

55. Backx, E., Coolens, K., Van den Bossche, J.L., Houbracken, I., Espinet, E., and Rooman, I. (2022). On the Origin of Pancreatic Cancer: Molecular Tumor Subtypes in Perspective of Exocrine Cell Plasticity. Cell. Mol. Gastroenterol. Hepatol. *13*, 1243–1253. https://doi.org/10.1016/j.jcmgh.2021.11.010.

56. Brassard, J.A., Tornabene, P., Kechele, D.O., Deng, L., Sneddon, J.B., Krishnamurthy, M., and Wells, J.M. (2025). Human pancreatic organoids derived from pluripotent stem cells recapitulate pancreatic organogenesis. Preprint at bioRxiv. https://doi.org/10.1101/2025.10.31.685661.

57. Schindelin, J., Arganda-Carreras, I., Frise, E., Kaynig, V., Longair, M., Pietzsch, T., Preibisch, S., Rueden, C., Saalfeld, S., Schmid, B., et al. (2012). Fiji: an open-source platform for biological-image analysis. Nat. Methods *9*, 676–682. https://doi.org/10.1038/nmeth.2019.

58. Berthold, M.R., Cebron, N., Dill, F., Gabriel, T.R., Kotter, T., Meinl, T., Ohl, P., Sieb, C., Thiel, K., and Wiswedel, B. (2007). KNIME: The Konstanz Information Miner. In Data Analysis, Machine Learning and Applications. Studies in Classification, Data Analysis, and Knowledge Organization, C. Preisach, H. Burkhardt, L. Schmidt-Thieme, and R. Decker, eds. (Springer), pp. 319–326. https://doi.org/10.1145/1656274.1656280.

59. Carpenter, A.E., Jones, T.R., Lamprecht, M.R., Clarke, C., Kang, I.H., Friman, O., Guertin, D.A., Chang, J.H., Lindquist, R.A., Moffat, J., et al. (2006). CellProfiler: image analysis software for identifying and quantifying cell phenotypes. Genome Biol. *7*, R100. https://doi.org/10.1186/gb-2006-7-10-r100.

60. Beydag-Tasöz, B.S., D'Costa, J.V., Hersemann, L., Lee, B.H., Luppino, F., Kim, Y.H., Zechner, C., and Grapin-Botton, A. (2023). Integrating single-cell imaging and RNA sequencing datasets links differentiation and morphogenetic dynamics of human pancreatic endocrine progenitors. Dev. Cell *58*, 2292–2308.e6. https://doi.org/10.1016/j.devcel.2023.07.019.

61. Zhu, Z., Verma, N., González, F., Shi, Z.D., and Huangfu, D. (2015). A CRISPR/Cas-Mediated Selection-free Knockin Strategy in Human Embryonic Stem Cells. Stem Cell Rep. *4*, 1103–1111. https://doi.org/10.1016/j.stemcr.2015.04.016.

62. Schmidt, U., Weigert, M., Broaddus, C., and Myers, G. (2018). Cell Detection with Star-Convex Polygons. In Medical Image Computing and Computer Assisted Intervention - Miccai 2018, A.F. Frangi, J.A. Schnabel, C. Davatzikos, C. Alberola-López, and G. Fichtinger, eds. (Springer International Publishing), pp. 265–273. https://doi.org/10.1007/978-3-030-00934-2_30.

63. Stöter, M., Janosch, A., Barsacchi, R., and Bickle, M. (2019). CellProfiler and KNIME: Open-Source Tools for High-Content Screening. Methods Mol. Biol. *1953*, 43–60. https://doi.org/10.1007/978-1-4939-9145-7_4.

64. Barber, C.B., Dobkin, D.P., and Huhdanpaa, H. (1996). The Quickhull algorithm for convex hulls. ACM Trans. Math. Softw. *22*, 469–483. https://doi.org/10.1145/235815.235821.

65. von Luxburg, U. (2007). A tutorial on spectral clustering. Stat. Comput. *17*, 395–416. https://doi.org/10.1007/s11222-007-9033-z.

66. Andrews, S. (2010). FastQC: A Quality Control Tool for High Throughput Sequence Data. https://www.bioinformatics.babraham.ac.uk/projects/fastqc/.

67. Cunningham, F., Achuthan, P., Akanni, W., Allen, J., Amode, M.R., Armean, I.M., Bennett, R., Bhai, J., Billis, K., Boddu, S., et al. (2019). Ensembl 2019. Nucleic Acids Res. *47*, D745–D751. https://doi.org/10.1093/nar/gky1113.

68. Dobin, A., Davis, C.A., Schlesinger, F., Drenkow, J., Zaleski, C., Jha, S., Batut, P., Chaisson, M., and Gingeras, T.R. (2013). STAR: ultrafast universal RNA-seq aligner. Bioinformatics *29*, 15–21. https://doi.org/10.1093/bioinformatics/bts635.

69. Love, M.I., Huber, W., and Anders, S. (2014). Moderated estimation of fold change and dispersion for RNA-seq data with DESeq2. Genome Biol. *15*, 550. https://doi.org/10.1186/s13059-014-0550-8.

70. Willert, K., Brown, J.D., Danenberg, E., Duncan, A.W., Weissman, I.L., Reya, T., Yates, J.R., and Nusse, R. (2003). Wnt proteins are lipid-modified and can act as stem cell growth factors. Nature *423*, 448–452. https://doi.org/10.1038/nature01611.

71. Barker, N., Huch, M., Kujala, P., van de Wetering, M., Snippert, H.J., van Es, J.H., Sato, T., Stange, D.E., Begthel, H., van den Born, M., et al. (2010). Lgr5(+ve) stem cells drive self-renewal in the stomach and build long-lived gastric units in vitro. Cell Stem Cell *6*, 25–36. https://doi.org/10.1016/j.stem.2009.11.013.

STAR★METHODS

KEY RESOURCES TABLE

REAGENT or RESOURCE	SOURCE	IDENTIFIER
Antibodies		
SOX17	BD Biosciences	Cat# 562205; RRID: AB_10893402
CXCR4	BD Biosciences	Cat# 560936; RRID: AB_10563070
PDX1	R&D Systems	Cat# AF2419; RRID: AB_355257
NKX6-1	BD Biosciences	Cat# 563338; RRID: AB_2738144
OCT4	BD Biosciences	Cat# 560329; RRID: AB_1645318
SSEA4	Thermo Fisher Scientific	Cat# MA1-021 D488; RRID: AB_2536688
TRA-1-60	Stem Cell Technologies	Cat# 60064PE; RRID: AB_2686905
C-Peptide	BD Biosciences	Cat# 565831; RRID: AB_2739371
Glucagon	BD Biosciences	Cat# 565891; RRID: AB_2739385
Chromogranin A	Agilent	Cat# M086901-2; RRID: AB_2081135
Neurogenin-3	R&D Systems	Cat# AF3444; RRID: AB_2149527
α-Amylase	Sigma-Aldrich	Cat# A8273; RRID: AB_258380
Trypsin	Millipore	Cat# MAB1482; RRID: AB_2237725
CPA2	Atlas Antibodies	Cat# HPA020342; RRID: AB_1846007
CPA1	Abcam	Cat# ab173283
SOX9	Millipore	Cat# AB5535; RRID: AB_2239761
GM130	BD Biosciences	Cat# 610823; RRID: AB_398142
Ezrin	Santa Cruz Biotechnology	Cat# sc-58758; RRID: AB_783303
ZO-1	Thermo Fisher Scientific	Cat# 40-2200; RRID: AB_2533456
PKC ζ	Santa Cruz Biotechnology	Cat# sc-17781; RRID: AB_628148
Alexa Fluor 568 Donkey Anti-Rabbit	Thermo Fisher Scientific	Cat# A100-42; RRID: AB_2534017
Alexa Fluor 488 Goat Anti-Mouse	Abcam	Cat# ab150113; RRID: AB_2576208
Alexa Fluor 488 Donkey Anti-Mouse	Jackson ImmunoResearch Labs	Cat# 715-545-151; RRID: AB_2341099
Alexa Fluor 488 Donkey Anti-Goat	Jackson ImmunoResearch Labs	Cat# 705-545-003; RRID: AB_2340428
Alexa Fluor 488 Donkey Anti-Rabbit	Jackson ImmunoResearch Labs	Cat# 711-545-152; RRID: AB_2313584
Chemicals, peptides, and recombinant proteins		
UEA1	Sigma-Aldrich	Cat# L9006
Hoechst-33342	Thermo Fischer Scientific	Cat# H1399
Phalloidin	Thermo Fischer Scientific	Cat# A22287
DAPI	Abcam	Cat# 228549
Ghost Dye 780	Cell signaling technology	Cat# 18452
mTeSR1	Stem cell technologies	Cat# 85850
hESC-Qualified Matrigel	Corning	Cat# 354277
TrypLE	Thermo Fischer Scientific	Cat# 12604013
ROCK inhibitor Y27632	Cell signaling	Cat# 13624
GFR - Matrigel	Corning	Cat# 356231
DMEM/F12 Glutamax	Thermo Fischer Scientific	Cat# 10565018
MCDB131	Life Technologies	Cat# 10372-019
Sodium bicarbonate	ThermoFisher	Cat# 25080094
Glutamax	ThermoFisher	Cat# 35050061
Glucose	Sigma-Aldrich	Cat# G6152
Fatty acid free bovine serum albumin	Lampire	Cat# 7500804
Ascorbic acid	Sigma-Aldrich	Cat# A4544
ITS-X	Thermo Fischer Scientific	Cat# 10524233

(*Continued on next page*)

Continued

REAGENT or RESOURCE	SOURCE	IDENTIFIER
CHIR99021	Axon	Cat# MC-1279
Activin A	Peprotech	Cat# 120-14
FGF 7	Peprotech	Cat# 100-19
Retinoic Acid	Sigma-Aldrich	Cat# R2625
Sant-1	Sigma-Aldrich	Cat# S4572
TPB	Millipore	Cat# 565740
FGF2	Peprotech	Cat# 100-18B
Pen/Strep	Thermo Fischer Scientific	Cat# 15070-063
Zinc Sulfate	Sigma	Cat# Z0251
GSiXX	Millipore	Cat# 565789
Heparin	Sigma-Aldrich	Cat# H3149-10KU
T3	Sigma-Aldrich	Cat# T6397-100MG
Alk5i	Santa Cruz	Cat# sc-221234B
B27	Thermo Fischer Scientific	Cat# 17504044
WNT-3a	Peprotech	Cat# 315-20
R-spondin1	Peprotech	Cat# 315-32
DAPT	Sigma-Aldrich	Cat# D5942
DMSO	Sigma-Aldrich	Cat# D8418
Triton X-100	Sigma-Aldrich	Cat# T8787
Rneasy micro kit	Qiagen	Cat# 74004
Random Primers	Invitrogen	Cat# 58875
Rnase OUT	Invitrogen	Cat# 10777-019
beta-mercaptoethanol	Fisher chemical	Cat# M/P200/05
Bovine serum Albumin	Lampire	Cat# 7500804
Formaldehyde	Thermo Fischer Scientific	Cat# 28908
Oligo (dT) 12-18 Primer	Invitrogen	Cat# 18418012
Carbacmoylcholine chloride	Sigma-Aldrich	Cat# C4382
HBSS 1X Buffer	gipco	Cat# 14025-092
Critical commercial assays		
Human Trypsin 1/PRSS1 ELISA Kit	RayBiotech	Cat# ELH-TRYP1
Amylase Assay Kit	Abcam	Cat# ab102523
Human Carboxypeptidase A2/CPA2 ELISA Kit	Sigma Aldrich	Cat# RAB1388
Deposited data		
Bulk RNA-sequencing dataset	This paper	ArrayExpress: E-MTAB-14625
Single-cell RNA-sequencing dataset	This paper	ArrayExpress: E-MTAB-16105
Experimental models: Cell lines		
H9	WiCell	Cat# WAe009-A
H1	WiCell	Cat# WAe001-A
IDP52555 #9	TU Dresden	Cat# CRTDi011-A RRID: CVCL_C1P8
WTC-11	Allen Institute	Cat# UCSFi001-A RRID: CVCL_Y803
PDX1-P2A-H2B-GFP and NEUROG3-P2A-tagRFP-T dual reporter	This paper	N/A
Oligonucleotides		
qPCR primers	See Table S3	This manuscript
Software and algorithms		
ImageJ (Fiji)	Schindelin et al.[57]	https://imagej.net/Fiji
KNIME (v.4.5)	Berthold et al.[58]	https://www.knime.com
Cell profiler	Carpenter et al.[59]	https://cellprofiler.org

(*Continued on next page*)

Continued

REAGENT or RESOURCE	SOURCE	IDENTIFIER
Prism 10 (v.10.5.0)	Graphpad	https://www.graphpad.com/
Adobe Illustrator 28.7.2	Adobe Inc	https://www.adobe.com/
Cell Ranger v6.1.0, v7.1.0	10x Genomics	https://support.10xgenomics.com/single-cell-gene-expression/software/pipelines/latest/what-is-cell-ranger
RStudio 2025.05.1	RStudio, PBC	https://www.rstudio.com/
FlowJo	BD (Becton, Dickinson & Company)	N/A
BioRender.com	BioRender	https://www.biorender.com

EXPERIMENTAL MODEL AND STUDY PARTICIPANT DETAILS

Human pluripotent stem cells

H9 and H1 hESC lines were obtained from WiCell. Reporters of PDX1:H2B-GFP and NEUROG3:tagRFP-T in H9 line (Figure S1A) and NEUROG3-TagRFP-T:EGFP in H1 line[60] were generated in house. The hESC lines were approved for use in this project by the Robert Koch Institute (AZ: 3.04.02/0148). Human induced PSC (hiPSC) lines, CRTD1 and CRTD11A, were obtained from Center for Regenerative Therapies Dresden (CRTD), and WTC11 from Allen Institute for Cell Science. All the reagent sources are indicated in Table S3. The hPSCs were expanded and maintained in mTeSR1medium (Stem Cell Technologies) on hESC-qualified Matrigel (Corning). Cells were maintained at 37°C and 5% CO_2, and the medium was changed daily. Upon reaching around 80% confluency, cells were dissociated with TrypLE (Thermo Fisher Scientific), counted with a cell counter (Countess II FL), and seeded at a density of 40,000 cells/cm^2. While passaging, the cells were supplemented with 10 μM ROCK inhibitor Y27632 (Cell Signaling) for the first 24 hours. The cells were regularly tested for Mycoplasma-free status.

METHOD DETAILS

Generation of PDX1 and NEUROG3 dual reporter hESC line

To label PP with H2B-GFP on *PDX1* locus and endocrine progenitor with tagRFP-T on *NEUROG3*, each locus was targeted by CRISPR/Cas9-mediated homology-directed repair. Reporter coding sequences of *P2A-H2B-GFP* and *P2A-tagRFP-T-NLS* were inserted before stop codon of *PDX1* and *NEUROG3* coding sequence, respectively (Figure S1A). We used previously reported guide RNA sequences for *PDX1*[61] and *NEUROG3*.[60] *PDX1* locus was targeted first by electroporation with 2 plasmids, one containing guide RNA and *CAS9* gene, and the other containing the targeting construct with homology arms, and then a clone, mono-allelic targeted, was selected for second targeting of *NEUROG3* locus. After the second targeting, a clone (L3-H9) was selected after differentiation validation. *NEUROG3* targeting was also mono-allelic.

Differentiation of hPSCs into PP cells

The step-wise protocol for differentiation based on the publication by Rezania et al.[20] was modified and adapted by us.[14] Briefly, hPSCs were passaged and cultured in 2D on plates coated with growth factor-reduced (GFR) Matrigel (Corning) at 1/30 dilution in DMEM/F12 Glutamax (Thermo Fisher Scientific). Cells were seeded at a density of 350,000 cells/cm^2 in mTeSR1 medium supplemented with 10 μM ROCK inhibitor for 24 hours before starting treatment with the differentiation media. Media changes were performed daily. The following media were used for differentiation. Stage 1 basal medium was composed of 1.5 g/L sodium bicarbonate, 1x Glutamax, 10 U/ml penicillin-streptomycin, 10 mM Glucose, and 0.5% fatty acid free bovine serum albumin (FAF-BSA) in MCDB 131 medium. The basal medium was supplemented with 3 μM CHIR and 100 ng/ml Activin A for day 1, 0.3 μM CHIR and 100 ng/ml Activin A for day 2, and 100 ng/ml Activin A for day 3. Stage 2 medium contained 1.5 g/L sodium bicarbonate, 1x Glutamax, 10 U/ml penicillin-streptomycin, 10 mM Glucose, 0.5% FAF-BSA, 0.25 mM ascorbic acid, and 50 ng/ml FGF7 in MCDB 131 medium and was used for 2 days. Stage 3 medium contained 2.5 g/L sodium bicarbonate, 1x Glutamax, 10 U/ml penicillin-streptomycin, 10 mM Glucose, 2% FAF-BSA, 0.25 mM ascorbic acid, 1:200 ITS-X, 1 μM retinoic acid, 0.25 μM Sant-1, 100 nM LDN193189, 200 nM TPB, and 50 ng/ml FGF7 in MCDB 131 medium and was used for 2 days. Stage 4 medium was composed of 2.5 g/L sodium bicarbonate, 1x Glutamax, 10 U/ml penicillin-streptomycin, 10 mM Glucose, 2% FAF-BSA, 0.25 mM ascorbic acid, 1:200 ITS-X, 0.1 μM retinoic acid, 0.25 μM Sant-1, 200 nM LDN193189, 100 nM TPB, and 2 ng/ml FGF7 in MCDB 131 medium and was used for 3 days. At stage 4 day 3, 97% of these cells expressed PDX1:H2B-GFP, a PP proxy, and 15% expressed NEUROG3:tagRFP-T, an endocrine progenitor proxy (Figures S1B–S1D).

Expansion and maintenance of hPSC-derived PP-organoids

Pancreatic progenitor cells at Stage 4 day 3 were harvested using TrypLE and seeded at a density of 40,000 cells in a 40 μl dome of 75% GFR Matrigel (1,000 cells/μl) per well on a 24-well plate. Upon solidification after 10 minute at 37°C, the Matrigel domes were

incubated in pancreatic epithelium (PE) medium[14] consisting of 1x B27 (Thermo Fischer Scientific), 64 ng/ml FGF2 (Peprotech), and 10 μM ROCK inhibitor in DMEM/F12-Glutamax at 37°C with 5% CO_2. Regular medium changes were performed every three days. Embedded in GFR Matrigel, PP cells cluster, proliferate, and self-organize to form PP-organoids. Organoids were passaged every ten days by dissociating into mostly single cells using TrypLE and re-seeding in 75% GFR Matrigel. Using this protocol, PP-organoids can be maintained in long-term cultures including freeze-and-thaw cycles. For quality controls, PP-organoids were regularly tested for expression of PDX1 (>99%) and NKX6-1 (>70%) by flow cytometry and also for Mycoplasma-free status.

High-content screening assay on PP-organoids

The screening was carried out in the High Throughput Technology Development Studio (TDS) in MPI-CBG. Dissociated cells from PDX1 and NEUROG3 dual reporter PP-organoids at day 10 were seeded in 384-well plates (Greiner, cat. 788986) as 3 μl suspensions in 75% GFR Matrigel at a density of 1,000 cells/μl using an automated dispenser Multidrop (Thermo Fischer Scientific). After 10 minutes of solidification at 37°C, 18 μl of PE medium was added per well.

We used in total 538 annotated small molecules (Table S1) from a set of compound libraries (StemSelect™ Small Molecule Regulators Library I, cat. 569744, InhibitorSelect™ Protein Kinase Inhibitor Library I, II, and III, cat. 539744, 539745, and 539746, Calbiochem, EMD Bioscience, Merck). These libraries contained compounds that are cell-permeable and annotated for inhibition of protein kinases or regulation of stem cell biology, and provided a good source targeting a diverse set of known biological pathways. These compounds were 10 mM stock solutions in DMSO. Each screening plate consisted of 28 wells of negative control DMSO, and the library compounds were distributed in three plates as one well per compound using an acoustic dispenser (Echo® 550, Labcyte). For compound treatments on day 3, the plates were first washed three times with DMEM/F12-Glutamax. Compounds were diluted to 2 μM in 2x concentrated PE medium without ROCK inhibitor, and 10 μl of PE medium was added into wells containing 10 μl of DMEM/F12-Glutamax to achieve a final concentration of 1 μM. Compound-containing media were exchanged on days 3, 5, 7, and 9 using an automated liquid handling workstation (Fluent 1080 and HydroSpeed, Tecan). The screen was performed with three biological replicates. The total duration of culture was 10 days, including 7 days with compounds to account for the slow development in human (considering cell cycle length of approximately 40 hours based on live imaging and differentiation of endocrine cells taking several days from progenitors to hormone expression[60]).

Fixation, immunostaining, and image acquisition

On day 10, plates were briefly centrifuged until the speed reached 1000 rpm to prevent wash away of objects, and the PP-organoids were fixed with 3.7% paraformaldehyde (PFA) for 15 minutes at room temperature (RT) by addition of the 2x concentrated fixation solution (7.4% PFA in PBS) using the WellMate (Thermo Fisher Scientific). After seven washes with 1x PBS using the HydroSpeed (Tecan), organoids were permeabilized with 0.5% Triton X-100 in PBS for 5 minutes at RT. Organoids were then incubated with 165 nM Phalloidin and 1.5 μg/ml DAPI in PBS containing 1% BSA for 3 hours at RT and stored in PBS containing 0.02% sodium azide at 4°C until imaging. Images were acquired for 4 fields and 4 z-positions (Z step 10 μm) for each well of the 384-well plates for 4 channels (DAPI: excitation 405 nm and emission 445/45 nm, PDX1:H2B-GFP: 488 nm and 525/50 nm, NEUROG3:tagRFP-T: 561 nm and 600/37 nm, and Phalloidin: 640 nm and 676/29 nm) with a 20X objective (NA 0.75) of an automated spinning disc microscope (Yokogawa CellVoyager CV7000).

Image segmentation and feature extraction

Images from 4 fields were stitched together with a FIJI macro[57] to generate one image for each z-position, 4 images per well. Cell nuclei were then segmented from each image using StarDist in the DAPI channel.[62] The nuclei labels and the images of all 4 channels were then imported into a CellProfiler[59] image analysis pipeline. We used a combination of the DAPI and Phalloidin signals to segment organoids in 2D for each z-plane. Nuclei objects identified by the StarDist segmentation were then related to the parent organoid. Finally, features describing shape, fluorescence intensities, and radial intensity distributions of both segmented organoid and nuclei were measured on each channel and exported as a csv file. Altogether, we extracted 353 features per organoid and 88 features per nucleus (Table S2). All macros, scripts, and pipelines were developed in the TDS.

Hit-selection by four analysis pipelines

KNIME (version 4.5)[58] was used for the following data analysis. Organoid objects touching the border as well as containing less than 7 nuclei, were excluded from the analysis. Additionally, objects from the lowest z-plane were not taken into account. Cell counts per well were expressed as percent of control (POC) with DMSO-treated wells as the control. Treatments resulting in more than 30% cell reduction were discarded from all hit lists to avoid toxic compounds. This may lead to an underestimation of hits, since some may have an effect on proliferation.

Well-mean analysis

Out of 218 features, scores of each feature were averaged per well (Table S2). These well-mean values were then normalized per plate by applying a POC normalization using control wells treated with DMSO only as reference. A second normalization step was then applied on the whole screen by calculating z-scores based on statistical descriptors of the distribution of DMSO-treated controls (z-score; $z = (x - \mu) / \sigma$, where x is the experimental value, and μ and σ are respectively the average and standard deviation of the normalizing control). We then applied a feature selection by first calculating a correlation matrix based on the Pearson correlation coefficient (PCC) between all features to eliminate redundancy. We clustered highly correlating features into 65 groups with

|PCC| > 0.5 by using hierarchical clustering with a distance measure being 1 - |PCC|. A curated selection of maximum one feature per group led us to 64 features to produce well-based, multiparametric profiles. We measured reproducibility between the profiles of the three runs by computing the PCC between the 2 different biological runs for each compound generating three sets of values for each comparison: run A and B, run A and C, run B and C. A compound was flagged as a hit when at least 2 out of 3 PCC $\geq$0.5. The rationale for this is that a hit compound is expected to generate a reproducible profile that should shift the PCC of that compound from the random correlation of the normalizing population.

Binning analysis/subpopulation analysis

The distributions of the values of the DMSO-treated control for a curated set of 34 different features related to size, shape, and morphology of the organoid objects (Table S2) were divided into three quantiles using the intervals [minimum value to 33rd percentile], [33rd percentile to 66th percentile], and [66th percentile to maximum].[63] Using these 3 bins set by DMSO control for each feature, we counted the number of organoids treated with compounds and determined their percentage in each bin. Finally, these values have been expressed as z-scores. For each feature bin combination, it was checked whether a compound showed an increase or decrease with z-score > |3| in at least two runs to consider it as a hit.

Network analysis

To determine shape and cell arrangement of each organoid, we used the centroid's xy locations of all corresponding nuclei as nodes. Then we performed a Delaunay triangulation to build a network.[64] Four features describing this network were extracted for each organoid and then averaged per well (Table S2). We applied the same normalization steps for each compound as in the well-mean analysis to retrieve z-scores per feature and the same 2 out of 3 hit selection criteria to build the hit list.

Morphological clustering

We built a multi-parametric profile using a curated set of 34 morphology features for each organoid, adding a binning analysis with 10 bins on the node distances of all nuclei (Table S2). All features were normalized as POC, followed by z-score. We then applied a UMAP projection of the resulting normalized morphology profiles to facilitate visualization. As a few features were only available on organoids with the presence of a clear lumen, the dataset was split into 2: one with a detectable lumen and the other without lumen. The following analysis was carried out on both sets, and the hit lists were merged. We clustered the UMAP-features of the organoids by applying spectral clustering[65] with k=6 for organoids with lumen and k=5 for organoids without lumen. The percentage of organoids per well assigned to each cluster was calculated and normalized by z-score. The hit selection followed the criteria described as in the binning analysis but applying z-score > |2.5| as a threshold.

Though we observed hits for features extracted based on the RFP channel, no significant changes in the expression of NEUROG3:tagRFP-T were observed in the nuclei. Several compounds with signals in this channel were excluded because they caused autofluorescence. These were generally detected in multiple channels (though some compounds fluoresced specifically in the red channel), and when checked in HeLa cells, which don't have the potential to differentiate into pancreatic endocrine cells, the same fluorescence was observed. Therefore, we did not pursue the hits from the RFP channel.

Dose response assay for hit validation

Eleven hit compounds were selected for validation (Table S1). Ten concentrations were chosen from a wide range of 0.1 μM to 10 μM, and assay was performed in two independent experiments with three replicates each. For the assay, imaging, and analyses, same protocols were applied as described above for the screen. We observed similar results from the two independent experiments, and data from one experiment are shown in Figures 2 and S3.

Bulk RNA-sequencing and data analysis

PDX1:H2B-GFP PP-organoids were treated with DMSO or 3 μM CHIR from day 3 onward with media changes performed on every alternate day. For CHIR-4days samples, CHIR was treated only from day 3 to day 7, followed by DMSO treatment from day 7 to day 10 to observe persistent effects after drug removal. Organoids were harvested as mostly single cells using TrypLE on day 4 and day 10 and snap frozen on dry ice for RNA extraction. For CHIR-treated conditions, three biological replicates were collected, while for DMSO conditions, four replicates were collected. Total RNA was extracted from the samples using the RNeasy micro kit (QIAGEN) by following manufacturer's guidelines, and quality assessment was done with Bioanalyzer (Agilent). Samples of RNA were sequenced with Illumina protocol at Dresden Concept Genome Center in CRTD.

Twenty nine paired-end (2x101) Illumina read data sets of sizes between 26.4 Mio and 37.9 Mio were processed. Illumina universal adapters were trimmed from both ends of the reads with Cutadapt v1.16 discarding reads trimmed to a length shorter than 19 nt. Quality of reads was assessed using FastQC 0.11.9.[66] Reads were mapped against the Homo sapiens genome reference assembly GRCh38, and genes of the Ensembl release v99[67] were quantified using STAR 2.7.3a.[68] Genes with at least 10 reads in at least one sample were input into the analysis of differential gene expression with DESeq2 v1.22.1.[69] Genes considered to be differentially expressed had to have an FDR<1%, considering p-values from the Wald test implemented in DESeq2 and a log2FC of min 2 (or max -2). The sets of differentially expressed genes were tested for Gene Ontology (GO) term (Kegg, GO, Reactome) enrichment with clusterProfiler v3.10.1 reporting hits at FDR<1%, and enriched Kegg pathways were visualized with pathview v1.20.0. Gene-set-enrichment analyses were performed with fgsea v1.8.0 and MSigDB v7.2.1 with the hallmark gene set (H), curated gene sets (C2), and ontology gene sets (C5) ranking all genes according to their log10-DESeq2-p-value (multiplied by -1 if the FC<1), reporting hits at FDR<1%. DESeq2, fgsea, and clusterProfiler were run in R 3.5.1.

Endocrine differentiation of PP- organoids

Based on Stage 5 and 6 of Rezania et al. protocol, PP-organoids were treated with CHIR from day 3 onward, changing medium on alternate days. On day 10, the organoids were washed with 1x PBS and treated with stage 5 medium[20] for three days, changing medium daily. On day 13, organoids were washed with 1x PBS and treated with stage 6 medium for 14 days, changing medium on alternate days. On stage 6 day 14, cells were harvested and analyzed by flow cytometry for C-PEP and GCG.

Stage 5 medium is composed of 1.5 g/L sodium bicarbonate, 1x Glutamax, 10 U/ml penicillin-streptomycin, 20 mM Glucose, 2% FAF-BSA, 1:200 ITS-X, 10 μM Zinc sulfate, 0.05 μM retinoic acid, 0.25 μM Sant-1, 100 nM LDN193189, 10 μM ALK5 inhibitor II, 1 μM T3, and 10 μg/ml Heparin in MCDB 131 medium. Stage 6 medium is composed of 1.5 g/L sodium bicarbonate, 1x Glutamax, 10 U/ml penicillin-streptomycin, 20 mM Glucose, 2% FAF-BSA, 1:200 ITS-X, 10 μM Zinc sulfate, 100 nM LDN193189, 10 μM ALK5 inhibitor II, 1 μM T3, 100 nM GSiXX, and 10 μg/ml Heparin in MCDB 131 medium.

WNT3A and RSPO1 treatment

From day 3 onward, PP-organoids were treated with PE medium supplemented with 30% WNT-conditioned medium along with WNT3A and RSPO1 (250 ng/ml and 750 ng/ml respectively). WNT-conditioned medium was a kind gift from Meritxell Huch.[70,71] DMSO and 3 μM CHIR treatments were used as controls, and media changes were performed as explained in the protocol for the screening assay. Samples were analyzed on day 10 by flow cytometry and whole-mount immunostaining.

Flow cytometry

Dissociated cells from PP-organoids were washed in 1x PBS and stained with Ghost Dye (Cell Signaling Technology) in PBS (1:1000) for 10 minutes at 4°C to stain dead cells before fixation. Cells were then washed with 1x PBS and fixed with 4% PFA for 10 minutes at RT. Fixed cells were washed with PBS and permeabilized for 20 minutes at 4°C with 0.2% Triton X-100 and 5% donkey serum in PBS. After permeabilization, cells were incubated with primary antibodies in the blocking buffer consisting of 0.1% Triton X-100 and 5% donkey serum in PBS overnight at 4°C. For the unconjugated antibodies, the cells were further incubated with the secondary antibodies in the blocking buffer for 45 minutes at RT. Antibody sources and concentrations are indicated in Table S3. Cells were then analyzed using FACSAria III (BD Biosciences), FCS Express 7 software (De Novo Software) and FlowJo 10.10.0 (BD Biosciences). Analysis was performed for at least 10,000 live cells. Representative data analysis and gating strategy are exemplified in Figures S1 and S5.

Whole-mount immunostaining of PP- organoids

PP-organoids were fixed with 4% PFA for 20 minutes at RT and washed three times with 1x PBS. Organoids were permeabilized with 0.5% Triton X-100 in PBS for 15 minutes at RT and incubated at RT with the blocking buffer made of 0.5% Triton X-100 and 3% BSA in PBS. Primary antibodies were added to the blocking buffer for 48 hours, followed by PBS washes three times and secondary antibodies in the blocking buffer for 48 hours. Organoids were cleared in 60% (vol/vol) glycerol and 2.5 M fructose solution overnight at 4°C. Antibody sources and concentrations are indicated in Table S3. Images were acquired using the Yokogawa CellVoyager CV7000 or Zeiss LSM 780 with Zen Black software and processed with ImageJ software.

Live imaging of PP-organoids

PP-organoids were cultured in 5 μl domes of 75% GFR Matrigel with 200 μl PE media in a 96-well plate. CHIR treatments were performed as explained above from day 3 to day 10. PP-organoids were imaged using Yokogawa CellVoyager CV7000 immediately after the compound addition on day 3, then day 7 and day 10. Images were acquired with the 20x objective in green channel for PDX1:H2B-GFP as well as bright field, covering a z-distance of 200 μm with a step-size of 20 μm.

Acinar differentiation protocol

PP-organoids were seeded on day 0 in 75% GFR Matrigel domes and treated with PE medium as described previously. On day 3, the organoids were treated with the modified PE medium containing 3 μM CHIR without FGF2 for seven days. 10 μM of SU5402, an inhibitor of FGFR, was also added along with CHIR in PE medium in the appropriately mentioned conditions. In some experiments, windows of treatment with the different combinations of WNT activation and FGF inhibition from day 3 to 7 or day 7 to 10 were also tested. Media changes were performed on days 5, 7, and 9. The spheres were harvested and fixed on day 10 for analysis. Experiments were performed with hESC- and hiPSC-derived PP-organoids from 3 cell lines.

Gene expression analysis by qPCR

The organoids were harvested as single cells after TrypLE treatment as described before and snap frozen as pellets in -80°C until processing. RNA was extracted using the QIAGEN micro kit by following the manufacturer instructions. First-strand cDNA synthesis was performed with Superscript III system (Thermo Fisher Scientific) using random or oligo dT primers (Thermo Fisher Scientific). Quantitative PCR was performed using SYBR-Green Master (Roche) on LightCycler 480 II instrument (Roche) for 96 well plates. PCR primers were selected based on published data or designed using NCBI primer design tool and validated for efficiency ranging between 95 and 105%. The primer sequences are listed in Table S3. Expression values for each gene were normalized against ACTB and then the DMSO control, using the delta CT and delta–delta CT methods, respectively.

Transmission Electron Microscopy

PP-organoids were collected and fixed in modified Karnovsky's fixative, in 1% glutaraldehyde and 2% paraformaldehyde in 100mM phosphate buffer (PB, pH 7.4) for 1 hour at RT followed by and an overnight incubation at 4°C. Samples were washed and further post-fixed in 1% aqueous OsO_4 solution containing 1.5% potassium ferrocyanide. After washing, samples were incubated and en bloc contrasted with 0.5% uranyl acetate/water overnight at 4°C. They were then washed, dehydrated in a graded ethanol series, infiltrated into EMBed 812 resin, and placed in embedding molds (Science Services GmbH). The embedded organoids were polymerized at 60 °C for 2 days. Ultrathin sections in 70 nm were cut with a Leica UCT ultramicrotome (Leica Microsystems) and collected on formvar-coated slot grids. The sections were post-stained with 1% uranyl acetate and 0.4% lead citrate. Electron micrographs were obtained at a 100 kV Tecnai12 transmission electron microscope (Thermo Fisher Scientific) with a digital camera (TVIPS TemCamF416) and analyzed with ImageJ.

Enzyme secretion stimulation and enzyme activity assays

PP-organoids were differentiated toward the acinar lineage as described above. On day 10, organoids were collected from Matrigel domes by removing the growth medium, washing three times with PBS, and incubating with TrypLE for 4 minutes at 37°C. TrypLE was neutralized by adding growth medium containing 10% FBS, followed by three PBS washes (centrifugation at 500 g for 3 minutes between washes). To stimulate enzyme secretion, 200 μl of 10 μM carbachol in HEPES buffer was added to each well, and cells were incubated for 2 hours at 37°C in a humidified incubator. Following stimulation, cell supernatants were collected and centrifuged at maximum speed for 2 minutes to remove debris. Cleared supernatants were snap-frozen on dry ice and stored at −80°C until further analysis. Concentrations and activities of enzymes (Amylase, Trypsin, and Carboxypeptidase A2) in the supernatants were determined by ELISA and enzyme activity assays according to the manufacturers' instructions. The source of assay kits are listed in Table S3.

Image segmentation and analysis of acinar-differentiated organoids

All analyses of images immunostained for acinar markers, amylase, and CPA2 were performed on CentOS Linux 7.4.1708 running Python 3.10.7. For nuclei segmentation, we used a pretrained 3D Cellpose model ('CP'), and trained it for an additional 100 epochs on an annotated subset of images from our own data (14 slices total from 3 different image volumes). During model prediction, we first smoothed the image with a Gaussian filter (sigma=2) and used a flow threshold of 0.4. After segmentation with Cellpose, we additionally removed segmented objects with an area less than 5000 pixels. For organoid segmentation, we first applied a Gaussian filter (sigma =10) for each image volume and then used the Triangle threshold from the scikit-image library to obtain an initial organoid mask. We then kept only the largest thresholded volume and applied post-processing steps of binary closing and erosion to further refine the mask. Image analysis was performed to quantify marker expression at the single-cell level. Individual cells were segmented based on nuclear staining, and mean fluorescence intensity was measured for each marker channel within the segmented regions. For each marker, mean intensity values were inspected and thresholded to classify cells as positive or negative. The number of positive and negative cells was then determined for each organoid. For each replicate, the proportion of marker-positive cells per organoid, and then the average value across organoids, was calculated.

Single-cell RNA-sequencing and analysis

PP-organoids (H1 hESC-derived) were differentiated toward the acinar lineage as described above. On day 10, organoids were dissociated into single cells using TrypLE, and cells were sorted into single cells by FACS based on cell viability staining by DAPI. The viability of single-cell suspensions was 90% (DMSO), 80% (CHIR), and 95% (CHIR noFGF2). For each condition, 27,000 cells were loaded onto a 10x Genomics Chromium GEM-X microfluidic chip (Single Cell 3' GEM-X, v4 chemistry), targeting ~20,000 captured cells per sample. cDNA amplification was performed for 10 cycles, followed by 0.6× SPRI purification. Libraries were sequenced on an Illumina NovaSeq 6000 (NovaSeq S4 v1.5, 4XP, 200 cycles). Base calling was performed with bcl2fastq2 (v2.20.0). Sequencing yielded 930,222,396 (DMSO), 857,521,610 (CHIR), and 699,688,065 (CHIR noFGF2) reads per sample.

Reads were demultiplexed and processed with Cell Ranger (v9.0.1, 10x Genomics) using parameters –chemistry=auto and –include-introns=true, aligned to the GRCh38 10x Genomics reference (refdata-gex-GRCh38-2024-A). Cell Ranger invoked Martian Runtime (v4.0.13), Python 3.10.8, and dependencies numpy (v1.26.4), scipy (v1.10.1), pysam (v0.21.0), h5py (v3.9.0), pandas (v2.1.4), and STAR (v2.7.2a). The minimum fraction of valid barcodes was 97.3%, and the fraction of valid UMIs reached 100%. Barcode-rank plots were inspected, and a second Cell Ranger run was executed with manually set expected cell numbers (–force-cells): 21,200 (DMSO), 16,000 (CHIR), and 20,200 (CHIR noFGF2). Mapping quality was high, with ≥93.3% of reads confidently mapped to the genome, ≥85% to the transcriptome, ≤3.6% mapping to intergenic regions, and ≥93.2% reads in cells. The median number of detected genes per cell was ≥4,163.

Spliced and unspliced transcript counts were derived using Velocyto (v0.17.17) applied to the Cell Ranger–generated BAM files. Output matrices were stored in MatrixMarket format (v2). Filtered count matrices (filtered_feature_bc_matrix) from the second Cell Ranger run were used for all downstream analyses.

Downstream analyses were performed in R (v4.0.5) using Seurat (v4.1.1), SeuratWrappers (v20210208), SingleCellExperiment (v1.12.0), SCTransform (v0.3.5), Scater (v1.18.6), VeloCyto.R (v0.6), scDblFinder (v1.15.1), and DoubletFinder (v2.0.3). Cells were filtered to retain those with ≥750 reads, ≥350 detected genes, and ≤15% mitochondrial read fraction; genes were required to be expressed in ≥3 cells. The mitochondrial gene fraction per cell was calculated from gene annotation. Normalization and variance

stabilization were performed with SCTransform, regressing out (1) mitochondrial read fraction, (2) S.Score, and (3) G2M.Score computed by Seurat's CellCycleScoring function. Normalized data were centered and scaled. No data integration was applied as it erased all biological variation previously observed in bulk sequencing. We note that data integration has been developed with the intent of comparing different populations with overlapping populations of cells where anchors can be easily extracted but not for perturbations leading to large shifts in cell identity. As all three conditions were processed in parallel, low technical noise is expected. This was confirmed by the fact that all endocrine cells from all conditions formed a distinct cluster and that part of the cells in CHIR+No FGF cluster with CHIR alone. Principal component analysis was performed on the 3,000 most variable genes. Cells were clustered using FindClusters (50 iterations, k = 75, entrees = 100, resolution = 0.1), and marker genes were identified with FindAllMarkers (only.pos = TRUE, min.pct = 0.25, logfc.threshold = 0.25, test. use = "wilcox", ba e = 2) after running PrepSCTFindMarkers. Visualization was performed in Seurat (v5.3.3) and ggplot2 (v3.5.2).

QUANTIFICATION AND STATISTICAL ANALYSIS

Statistical tests were done using KNIME 4.5 or GraphPad Prism 10. *p*-values were calculated using a one sample t-test or two way--ANOVA. For the screen data, z-scores were converted to *p*-values based on two-tailed hypothesis. Significance was defined as $*p<0.05$, $**p<0.01$, $***p<0.001$, $****p<0.0001$ and $*****p<0.00001$. Experimental repeats are indicated in the figure legends. "N" denotes the number of independent experiments (biological repeats), and "n" the total number of measurements. All data are presented as mean ± standard deviation.